Hydrothermal Alteration on Composite Volcanoes –Mineralogy, Hyperspectral Imaging and Aeromagnetic Study of Mt Ruapehu, New Zealand

Gabor Kereszturi[1*], Lauren N. Schaefer[2,3], Craig Miller[4], Stuart Mead[1]

[1]Volcanic Risk Solutions, Massey University, Palmerston North, 4474, New Zealand
[2]School of Earth and Environment, University of Canterbury, Christchurch, 8140, New Zealand
[3]U.S. Geological Survey, 1711 Illinois St., Golden, CO, 80401, USA
[4]GNS Science, Wairakei Research Centre, Taupo, 3353, New Zealand

*Corresponding author: Gabor Kereszturi (G.Kereszturi@massey.ac.nz)

Key Points:

- Surface weathering and hydrothermal mineralogy was constrained using VNIR and SWIR reflectance spectroscopy and SEM-EDS analysis
- Combination of airborne hyperspectral image analysis and aeromagnetic data inversion mapped surface and buried hydrothermal alteration on Mt Ruapehu volcano
- Complex hydrothermal evolution of Mt Ruapehu is revealed using geophysical imaging techniques combined with surface alteration mineralogy

Abstract

Prolonged volcanic activity can induce surface weathering and hydrothermal alteration that is a primary control on edifice instability, posing a complex hazard with its challenges to accurately forecast and mitigate. This study uses a frequently active composite volcano, Mt Ruapehu, New Zealand, to develop a conceptual model of surface weathering and hydrothermal alteration applicable to long-lived composite volcanoes. The rock samples were classified as non-altered, supergene argillic alteration, intermediate argillic alteration, and advanced argillic alteration. The first two classes have a paragenesis that is consistent with surficial infiltration and circulation of the low-temperature (<40 °C) neutral to mildly acidic fluids, inducing chemical weathering and formation of weathering rims on rock surfaces. The intermediate and advanced argillic alterations are formed from hotter (≥100 °C) hydrothermal fluids with lower pH, interacting with the andesitic to dacitic host rocks. The distribution of weathering and hydrothermal alteration has been mapped with airborne hyperspectral imaging through image classification, while aeromagnetic data inversion was used to map alteration to several hundred meters depth. The joint use of hyperspectral imaging complements the geophysical methods since it can numerically identify hydrothermal alteration style. This study established a conceptual model of hydrothermal alteration history of Mt Ruapehu, exemplifying a long-lived and nested active and ancient hydrothermal system. This study highlights the need to combine mineralogical information, geophysical techniques and remote sensing to distinguish between current and ancient hydrothermal and supergene alteration systems, to indicate the most likely areas of future debris avalanche initiation.

Plain Language Summary

Groundwater heated by shallow intrusive bodies beneath an volcano can contribute heat and magmatic gasses to the groundwater. The magmatic contributions, such as sulfur dioxide, can make groundwater acidic. When the acidic groundwater rises to the surface, it chemically interacts and changes volcanic rocks, leading to hydrothermal alteration. This alteration can weaken rocks by depositing clay minerals in fractures and pore-space, and in turn inducing edifice collapse hazards. This contribution integrates mineralogy, hyperspectral remote sensing and geophysical methods to understand the hydrothermal alteration history of a seemingly unaltered volcano, Mt Ruapehu, New Zealand. Ground sampling indicates alteration mineralogy is dominated by sulfides and sulfates. Hyperspectral remote sensing measures reflected sunlight from the Earth's surface, allowing quantitative discrimination and mapping of surface minerals at high resolution using image classification. The surface alteration was jointly analyzed with the aeromagnetic inversion models to understand underground hydrothermal alteration. Aeromagnetic data is sensitive to iron-bearing, magnetic minerals that are often dissolved by hydrothermal fluids, leaving low magnetic anomalies. The combination of these methods allowed a detailed conceptualization of alteration history of Mt Ruapehu during the last 200,000 years. This conceptual model will be used to assess natural hazards associated with flank collapses using numerical models.

1. Introduction

Interaction of the magmatic heat and gasses (e.g. mostly Cl, SO_2, H_2O, CO_2) drives infiltrating surface and circulating groundwater to ascend through the volcanic host rocks while leaching primary alkali (Na, K) and alkaline earth metals (Mg, Ca), replacing existing mineral phases and precipitating new secondary minerals at shallower depths (Ganino et al., 2019; Hynek et al., 2013; Rowe and Brantley, 1993; Rye et al., 1992). Acid-sulfate alteration forms typical intermediate and advanced argillic mineral assemblages, including phyllosilicates (Dill, 2016; Hynek et al., 2013), sulfates (Rye et al., 1992; Zimbelman et al., 2005), sulfides, and native sulfur (Inostroza et al., 2020; Piochi et al., 2015). The majority of hydrothermal alteration occurs beneath the surface in hypogene conditions; however, mineral assemblages formed under hypogene conditions are often subject to supergene weathering and erosion which can replace some of the metastable hydrothermal minerals under atmospheric pressure and temperature conditions, including dickite, anhydrite, sulfur and pyrite (Fernández-Caliani et al., 2004; John et al., 2008; Scott, 1990; Zimbelman et al., 2005). This commonly results in mineral imprinting, making interpretations of the original hydrothermal condition, fluid composition and pH challenging, particularly on complex and long-lived volcanic systems.

Hydrothermal alteration results in economic resources, such as Au, Ag, and base metal deposits; however, it also changes rock mechanical and geotechnical properties (del Potro and Hürlimann, 2009; Pola et al., 2014), promoting flank instability (Finn et al., 2001; Heap et al., 2015; John et al., 2008; López and Williams, 1993; Norini et al., 2020; Schaefer et al., 2015) and increasing the likelihood of phreatic eruptions (Mayer et al., 2017; Pardo et al., 2014). Hydrothermal alteration primarily reduces rock strength (del Potro and Hürlimann, 2009; Farquharson et al., 2019), and changes permeability within the volcanic edifice (Mordensky et al., 2019b), which may locally elevate pore-pressure promoting edifice flank instabilities (Ball et al., 2018; Collard et al., 2020; Reid, 2004). Flank instabilities, and the resulting mass flow events triggered by gravity, weather events, volcanic eruptions, magmatic intrusions, and earthquakes (Capra, 2006; Procter et al., 2014; Schaefer et al., 2018) can result in far-reaching and potentially dangerous volcanic hazards downstream from volcanoes (Finn et al., 2001).

Geological mapping and quantification of hydrothermal alteration in volcanic systems have traditionally been carried out using ground and field geological mapping, combined with Scanning Electron Microscopy (SEM), X-Ray Diffraction (XRD) and X-ray fluorescence (XRF), and isotope and fluid inclusions studies, among others, to constrain the paragenesis of the alteration mineral suites (Ball et al., 2013; Christenson and Wood, 1993; John et al., 2008; Nuñez-Hernández et al., 2020; Piochi et al., 2019; Rye, 2005; Zimbelman et al., 2005). Multispectral satellite remote sensing in the Visible and Near Infrared (VNIR – 300-1000 nm) and Shortwave Infrared (SWIR – 1000-2500 nm) is often used to upscale mapping efforts, using Landsat series (Mia and Fujimitsu, 2012; Wright et al., 2001), Advanced Spaceborne Thermal Emission and Reflection Radiometer – ASTER (Galvão et al., 2005; Rowan and Mars, 2003), and WorldView constellation (Kruse et al., 2015). Lately, hyperspectral remote sensing is becoming available for mineral alteration mapping, improving the differentiation among key indicator minerals such as alunite, jarosite, kaolinite, montmorillonite and illite, and mica, offering a cost-effective but highly sophisticated technological solution (Carrino et al., 2018; Crosta et al., 1998; Crowley et al., 2003; Hellman and Ramsey, 2004; Kereszturi et al., 2018; Swayze et al., 2014; van der Meer, 2004). However, optical remote sensing approaches are limited to quantify only the surface manifestation of hydrothermal alteration and weathering, hampering these techniques to be used for hazard assessment of geophysical mass flow.

Complementing ground and remote sensing methods, geophysical techniques, including electromagnetic resistivity, gravity and aeromagnetic surveys (Finn et al., 2018; Miller and Williams-Jones, 2016), magnetotelluric surveys (Abdallah et al., 2020; Bowles-Martinez and Schultz, 2020; Jones et al., 2008; Matsunaga et al., 2020), seismicity (Pu et al., 2020), moun imaging (Le Gonidec et al., 2019) have also been used to infer internal architecture, and locate hydrothermal fluids and zones of demagnetization of the host rock. These survey methods are often complemented with numerical methods and spring and gas chemistry data to gain insights into the thermal and chemical evolution of shallow magmatic-hydrothermal systems (Berlo et al., 2020; Collard et al., 2020; Gresse et al., 2018; Miller et al., 2020a). Therefore, geophysical inversion and numerical methods can add the depth component to quantify hydrothermal alteration processes and volumes of altered rock masses, contributing important inputs to mass flow initiation and run-out models and hazard assessment (Finn et al., 2018; Finn et al., 2001; Rosas-Carbajal et al., 2016).

Both geophysical and optical remote sensing approaches have been demonstrated to be useful for mapping hydrothermal alteration products. However, the joint use of such methods is seldomly presented on composite volcanoes to fingerprint hydrothermal alteration processes on the surface and depth. This study aims, therefore, to explore the hydrothermal alteration history of a long-lived and complex andesitic composite volcano, Mt Ruapehu, New Zealand, using a novel combination of mineralogical, hyperspectral and geophysical imaging techniques. The detailed reconstruction of the hydrothermal alteration history and conceptual model can provide inputs to predict edifice instabilities and associated geophysical mass flow hazards around composite volcanoes.

2. Geological Setting

The southern part of the Taupo Volcanic Zone contains Mt Tongariro and Mt Ruapehu volcanoes and several smaller inactive volcanic centers, which collectively form the Tongariro Volcanic Complex (Fig. 1A). Mt Ruapehu, 2797 m a.s.l. and 110 km^3, is a frequently active andesite-dacite volcano (Hackett and Houghton, 1989), formed via back-arc volcanism behind an active subduction zone at the Australian and Pacific plate boundary (e.g. Stern et al., 2006; Wallace et al., 2004).

The first deposit originated from Mt Ruapehu is dated to around 340 ky ago (Hackett and Houghton, 1989; Price et al., 2012), preserved within distal catchment areas as river aggradation terraces (e.g. Tost et al., 2015). The stratigraphic framework of Mt Ruapehu comprises four formations, on the basis of geochronology, geochemistry and stratigraphic relationships, pinpointing distinct spatial-temporal stages of volcano evolution (Fig. 1A): Te Herenga (200 to 150 ka), Wahianoa (166-80 ka), Mangawhero (50-15 ka) and Whakapapa (<15 ka) formations (Conway et al., 2016; Gamble et al., 2003; Hackett and Houghton, 1989; Price et al., 2012; Townsend et al., 2017). The only major hiatus in activity is from 80 to 50 ky, which was a period of erosion and edifice instabilities (Townsend et al., 2017).

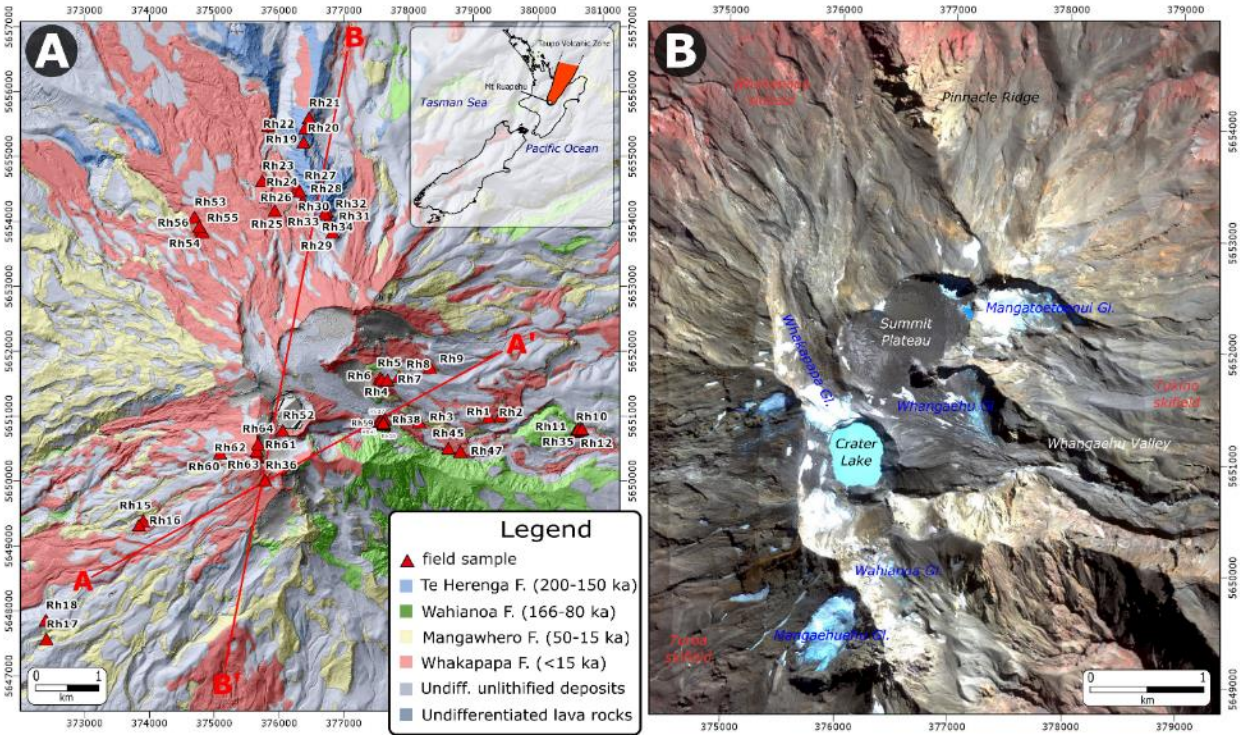

Figure 1. (A) A simplified geological map of Mt Ruapehu, with the major geological formations after Townsend et al. (Townsend et al., 2017), draped over a hillshade model. The red triangles show the location of the physical samples collected in this study. (B) Infrared-colored composite image of the airborne hyperspectral imagery (R = 860.1 nm; G = 650.2 nm, B = 550.7 nm) with the locations mentioned in the text.

The whole-rock chemistry of Mt Ruapehu varies between basaltic andesite and dacites (Price et al., 2012). Rock textures at Mt Ruapehu are mainly porphyritic with phenocryst abundances averaging 35-55% (Price et al., 2012); however, some lava flows exhibit aphyric texture. The main phenocrysts in decreasing abundance are plagioclase (8-39 vol%), clinopyroxene (2-14 vol%), orthopyroxene (2-10 vol%), magnetite and titanomagnetite (1-6 vol%), as well as rare occurrences of olivine and amphiboles (Conway et al., 2018; Gamble et al., 1999; Graham and Hackett, 1987; Nakagawa et al., 1999; Price et al., 2012). See detailed summary in Table S1. The composition of the plagioclase and pyroxene phenocrysts show differences within the main lithologic units, highlighting a changing magmatic source and edifice evolution over time (Conway et al., 2018; Kilgour et al., 2013).

The current volcanic edifice is made of mostly lava flows and their auto-breccias, with minor exposed volcaniclastic deposits, such as lahar, debris avalanche and tephra fall deposits (Conway et al., 2016; Townsend et al., 2017). Such lava flows seldomly reach the extensive ring plain around the volcanoes which preserved an extensive record of debris flows, debris avalanches, hyper-concentrated flows with interbedded local andesitic and distal rhyolitic tephras (Donoghue and Neall, 1996; Pardo et al., 2012). Mt Ruapehu has produced 8-10 debris avalanches in the last 340 ky. The last two debris avalanches, Murimotu (9.5 ky) and Mangaio (4.6 ky) affected the NW and E sides, and reached ca. 15 and 25 km distance, respectively (Donoghue and Neall, 2001; Palmer and Neall, 1989).

A recent period of magmatic activity occurred between September and November 1995, and June and July 1996, producing mild Strombolian to violent phreatomagmatic eruptions (Cronin et al., 1997; Johnston et al., 2000; Nakagawa et al., 1999). The 1995-96 and 2007 eruptions disrupted the top parts of the hydrothermal system, providing otherwise inaccessible samples to characterize the physico-chemical state of the host rock and hydrothermal under the currently active Crater Lake (Christenson, 2000; Christenson et al., 2010; Christenson and Wood, 1993).

A previous magnetotelluric survey data was used to model the electrical resistivity structure of the upper flanks of Mt Ruapehu and its surroundings, indicating hydrothermally altered rocks located under the Summit Plateau (Ingham et al., 2009; Jones et al., 2008). Two higher resistivity zones (20-60 Ω m) located under the Northern part of the Summit plateau at 200-500 m, and 1000-1500 m depths, are interpreted to be due to changing alteration mineralogy from smectite-illite to chlorite-rich zones (Jones et al., 2008). This region was further imaged using aeromagnetic data inversion and interpreted to be smaller demagnetized zones, corresponding to hydrothermally altered rocks (Miller et al., 2020b). Besides Crater Lake, there is no known active hydrothermal system on Mt Ruapehu; however, older parts of the Mt Ruapehu indicates extensive hydrothermal alteration history, such as the Te Herenga Formation (Mordensky et al., 2019a).

3. Methods and Materials

3.1. Field Sampling and Lab Analytics

A total of 64 samples were collected during field campaigns between 2017 and 2019 (Fig. 1A). The samples are from lava flows (interior core and brecciated exterior), and tephra deposits and range from fresh to extensively altered. Some of the samples represent subsurface lithologies (upper 200 m), brought to the surface by the 2007 eruption induced lahar and the ballistics from the 1995-96 eruption. Samples were analyzed using lab-based reflected light spectroscopy, optical microscopy, and Scanning Electron Microscope (SEM) equipped with Energy Dispersive X-ray spectroscopy (EDS).

Lab-based reflectance spectroscopy was completed using a FieldSpec 4 Hi-Res spectroradiometer, equipped with a Hi-Brightness contact probe with a sampling footprint of 10 mm in diameter. The samples were air-dried at 40 °C for 24 hours before analysis to ensure samples were dry. The spectral readings were calibrated against a white Spectralon Diffuse Reflectance Standard. Spectra measurements were completed at 2-7 “spots” on each specimen, which assured representative sampling of the variation of the alteration within each sample. Each of these “spots” included at least 100 spectral measurements. All spectral measurements were then averaged using View Spec Pro software and later exported into a spectral library. When an alteration rim/crust was present on a sample, the interior and outer rim were analyzed separately. The averaged spectral reflectance was used to recognize the typical mineral association within the samples using continuum removed spectral curves (Clark and Roush, 1984). The wavelength of the absorption features (i.e. reflectance lows) was matched manually with the USGS Spectral Library Version 7 (Kokaly et al., 2017), as well as automatically using a Spectral Feature Fitting approach implemented in ENVI (Clark et al., 1990). A list of key spectral absorption features and descriptions are summarized in Table S2.

A subset of the samples was prepared for thin section, Scanning Electron Microscope (SEM) and Energy-dispersive X-ray Spectroscopy (EDS) for petrographic and geochemical analysis. These samples were cut, mounted onto glass slides and then ground to 30 µm and polished for optical microscopy, while other samples were ground to about 100 µm, and polished for SEM-

EDS analysis. The latter batch was carbon-coated and imaged using ThermoFisher Scientific™ FEI Quanta 200 Environmental Scanning Electron Microscope operated in Back-Scattered Electron (BSE) mode under accelerating voltage of 20 kV, with a working distance of 10 mm, at the Massey University's Manawatu Imaging Centre. BSE equipped with an EDAX-EDS system was used to identify element abundance to characterize rock alteration types and secondary mineralogy.

Magnetic susceptibility measurements were made on tephra and rock outcrop and hand specimens using a Terraplus KT-10 v2 magnetic susceptibility meter. The Terraplus was held in direct contact with the surface of each sample on a flat surface if possible, measured three times, and averaged to produce one value per sample.

3.2. Hyperspectral Imaging Surveys

Aerial surveys were completed using a Cessna 185 survey aircraft, with two integrated imaging systems onboard, between 10:25-12:45 NZST on 31 March 2018. The survey aircraft hosted a Specim AisaFENIX hyperspectral imaging system, alongside a Nikon D810 digital single-lens reflex camera with a 35 mm lens. The aircraft was flown at 3300 feet above the ground, capturing N-S orientation survey strips with 410 m line spacing.

The GPS-tagged digital photos had a maximum ground resolution of 13.9 cm. They were captured with 60% side- and forward overlaps. This imagery was to create a structure-from-motion Digital Surface Model (James and Robson, 2012; Westoby et al., 2012). The RAW imagery was converted to JPEG to perform the initial image matching in Pix4D software package. This was followed by georectification using 3D ground control points from high-resolution aerial photographs, taken in 2016, from Land Information New Zealand, and existing 10 m terrain models captured by Horizons Regional Council. This workflow resulted in a 50 cm bare-ground Digital Terrain Model (DTM), and 50 cm an orthophoto mosaic. Both were used to process and co-register the coarser-resolution hyperspectral imagery.

The AisaFENIX hyperspectral sensor is a push-broom, full-spectrum imaging system, along with an Oxford Survey+ Global Position System and Inertial Measurement Unit (Pullanagari et al., 2016). It captures reflected light between 377 and 2500 nm with variable spectral sampling intervals of 3.3-5.7 nm for VNIR bands and of 11 nm for the SWIR bands. It has a full-width-at-half-maximum between 3.2–12.2 nm. The Field of View is 32.2°, while the Instantaneous Field of View is 0.084°. The data has 448 spectral bands with a ground resolution of 1.5 m. The raw hyperspectral sensor measurements are converted to radiance ($W \cdot sr^{-1} \cdot m^{-2}$) using sensor-specific gain and offset values, provided by Specim Ltd, Finland. The radiance imagery is corrected for atmospheric effect using ATCOR-4 algorithm, performed on the raw imaging geometry (Richter and Schläpfer, 2002). The atmospheric correction parameters were identical to Kereszturi et al. (2018). The atmospherically corrected imagery represents surface reflectance values that can be compared with spectral libraries or with other survey data. The atmospherically corrected reflectance imagery was geocoded using PARGE (Schläpfer and Richter, 2002). Since the hyperspectral imagery was captured with standard GPS positioning (±6-8 m at 2σ), there are often misalignments and shift to *X* and *Y* directions by up to 10 m. This was reduced by co-registering all image strips to the high-resolution orthophoto. The Root Mean Squared Error of the co-registration was around <2 m. The imagery was mosaiced, and then spectrally smoothed to reduce noise.

The hyperspectral imagery can be used to map the surface spatial distribution of hydrothermally altered mineral packages (Carrino et al., 2018; Murphy et al., 2015; Rogge et al., 2014; Zabcic et al., 2014), using supervised image classification. This requires training and validation data to be identified. This study uses the hydrothermal alteration mineralogy and their sample location as well as field observations to develop training and validation populations, split at 50-50% for the supervised image classification. The total area was split into 5 rock alteration classes based on the alteration mineralogy (e.g. unconsolidated-unaltered, unaltered lava rocks, supergene argillic alteration, intermediate-, and advanced argillic alteration types), and 3 general classes (e.g. water, ice/glacier and shadow). The alteration types were based on the observed mineralogy in the collected samples. This study used Random Forest classification (Breiman, 2001), which is effective at reducing overfits due to highly co-linear data (i.e. hyperspectral imagery), while also being time-efficient, and yielding accurate results (Belgiu and Drăguţ, 2016; Kereszturi et al., 2018; Pal, 2005). Random Forest algorithm constructs decision trees using a subset of the training data and variables (i.e. spectral bands). Each tree is expanded until either the maximum number of input data used or they reached the minimum impurity value (i.e. 0), based on the calculated Gini impurity measure (Belgiu and Drăguţ, 2016; Breiman, 2001). In this study, the total number of tree models was 500, and at each split of the inputs, the square-root of input total variables (i.e. 21 bands) was used. The class values were assigned using majority voting procedure based on the individual tree's prediction. The resultant classification image was assessed using independent validation population, through calculating the overall accuracy and an error matrix of user's and producer's accuracies (Liu et al., 2007).

3.3. Helicopter borne Aeromagnetic Survey

A helicopter-based aeromagnetic survey was carried out two weeks after the hyperspectral surveys in April 2018. We collected 800 km of magnetic data with a Geometrics G822A Cs-vapor magnetometer flown at 50 m above ground at 250 m-spaced flight lines which we reduced to 125 m over the Pinnacles and Summit Plateau. Sampling the magnetic field at 10 Hz results in a magnetic field value every 2 m. We corrected for diurnal variations using a local base magnetometer outside the survey region and subtracted the International Geomagnetic Reference Field (IGRF) at each data point location using the IGRF 2005 model. The data were levelled using widely spaced tie lies to minimize cross over difference and were gridded for visualization at 20 % of the line spacing using a minimum curvature algorithm (see Miller et al. (2020b) for full details).

To map the spatial distribution of magnetic and non-magnetic rocks within Mt Ruapehu volcano, a magnetic vector inversion algorithm was used, which is implemented in the SimPEG inversion framework package (Cockett et al., 2015; Fournier et al., 2020; Miller et al., 2020b). The inversion accounts for remanent magnetism, common in volcanic rocks, by solving for both the amplitude and direction of magnetization. The inversion returns a 3D model of apparent susceptibility that we interpret in terms of altered versus fresh rocks, where high apparent susceptibility typically reflects unaltered rocks and low apparent susceptibility increasingly altered rocks. The inversion model uses a mesh with minimum dimensions of 50×50×25 m or 25×25×10 m over the Pinnacle Ridge and Summit Plateau areas. The typical apparent susceptibility values recorded from the model range from 0 to 0.05 SI, which can be interpreted as a degree of hydrothermal alteration, from fully demagnetized/altered to magnetic/fresh rocks, respectively (Miller et al., 2020b).

4. Results

4.1. Alteration Mineralogy

Based on the physical samples were grouped based on their alteration mineral phases mineralogy: (1) non-altered rock/deposits with minor surface weathering, (2) supergene argillic alteration with weathering rim, (3) intermediate argillic alteration and superimposed surface weathering, and (4) advanced argillic alteration. This classification scheme is based on the presence and absence of alteration minerals that represent distinct physico-chemical alteration domains (John et al., 2019; John et al., 2008; Rye et al., 1992; Zimbelman et al., 2005).

4.1.1. Non-altered Lithologies with minor weathering

The non-altered lithologies frequently occur on blocky lava flows with auto-brecciated horizons (Figs 2A-B) and are characterized by absorption at wavelengths of 420, 480, 500-560, 1912, 2200 nm, and occasionally ±660, ±950, ±1430 nm (e.g. rh1, rh2, rh4-9). In thin section, the studied samples show mostly fresh porphyritic, and rarely aphyric and vitrophyric textures (Fis 2C-D). The samples have about 30-50 vol% phenocrysts of plagioclase, clinopyroxene and orthopyroxene, various amounts of Ti-rich magnetite, and rarely olivine (Figs 2C-D). The phenocrysts are often euhedral to subhedral and occasionally show glomerophyric appearance. Some of the phenocrysts show chemical zonation, melt inclusions and sharp crystal boundaries, indicating their unaltered and fresh origin. The groundmass is made of tabular plagioclase microlites and volcanic glass. Some samples have a thin (≤1 mm) yellow to brown colored alteration rim, in which the groundmass is often replaced by secondary minerals, including phyllosilicates. The phenocryst phase appears to be still fresh (Figs 2C-D), but rarely Ti-magnetite crystals show trellis-type lamellae structures, especially within weathering rims. This can potentially indicate either high-temperature exsolution and oxidation during cooling (e.g. Buddington and Lindsley, 1964; Tan et al., 2016) or due to hydrothermal alteration and surface weathering (e.g. van Hinsberg et al., 2010). The measured magnetic susceptibilities of this group range from 0.002 to 0.03 SI (Miller et al., 2020b), reflecting a wide range of variability of the (Ti-) magnetite content on Mt Ruapehu (Price et al., 2012).

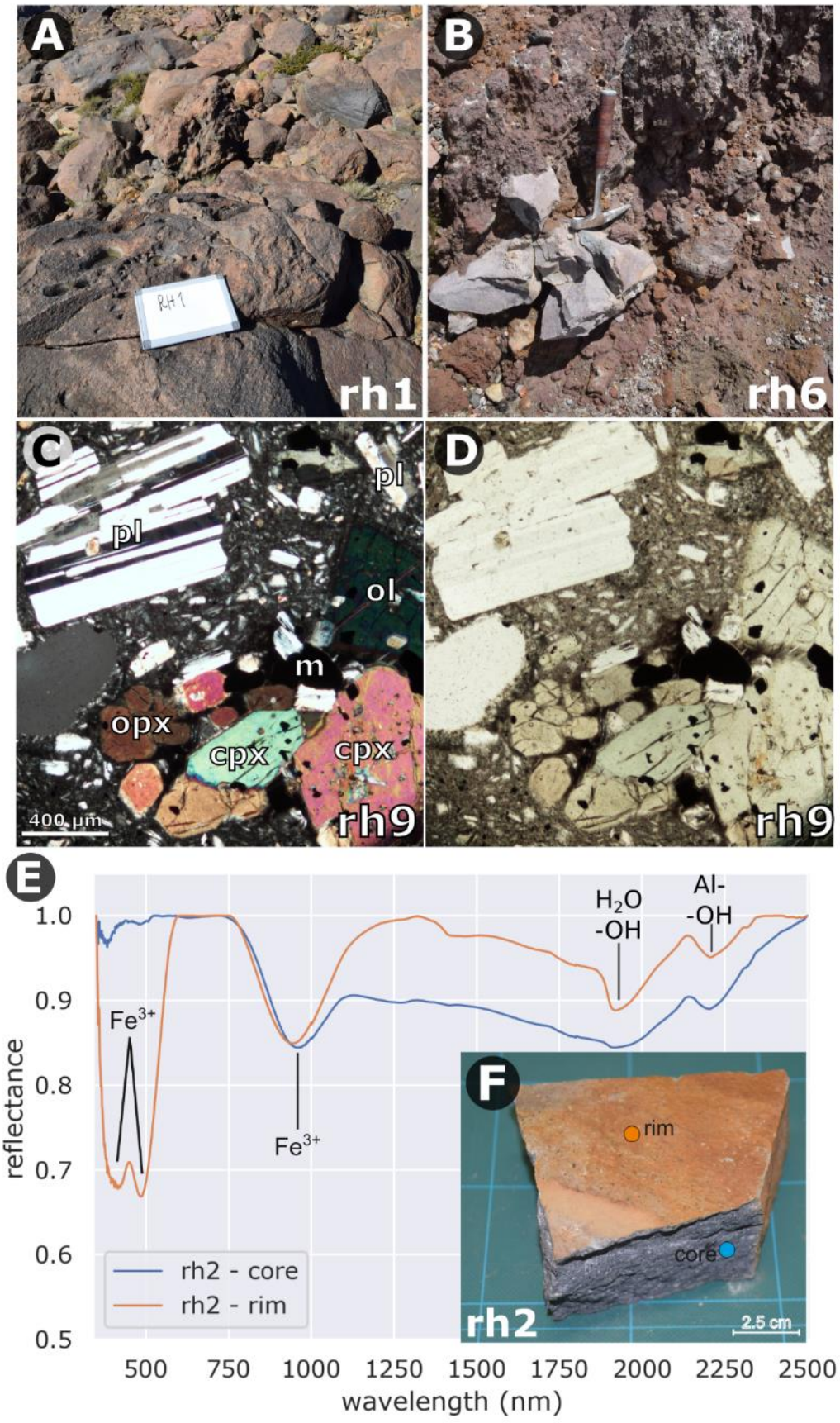
A
RH1
rh1
B
rh6
C
pl
pl
ol
m
opx
cpx
cpx
400 µm
rh9
D
rh9
E
1.0
0.9
0.8
0.7
0.6
0.5
reflectance
Fe3+
Fe3+
H2O
-OH
Al-
-OH
rh2 - core
rh2 - rim
500
750
1000
1250
1500
1750
2000
2250
2500
wavelength (nm)
F
rim
core
rh2
2.5 cm

Figure 2. (A-B) Field photos of the fresh non-altered outcrop, and (C-D) thin section photographs of a fresh lava sample under cross-polarized light in C and plane-polarized light in D. Abbreviations: plg – plagioclase, opx – orthopyroxene, cpx – clinopyroxene, o – olivine, m – magnetite. (E) Spectral reflectance profiles of the inner core and rim of rh2 sample (F). The main elements and element-bonds are indicated the cause of the light absorption. The reflectance values have been normalized using continuum removal (Clark and Roush, 1984).

The position of the absorption in the VNIR and SWIR regions can be explained by oxidation of primary mineralogy (e.g. magnetite, pyroxene) and limited, but detectable development of secondary clay minerals (e.g. mostly in the groundmass), with and without alteration rims (e.g. Fig. 2E). Such absorption is due to the presence of hydrous phases (e.g. 1430, 1912 and 2200-2350 nm, and state transition from Fe^{2+} to Fe^{3+} (e.g. between 400-1000 nm) (Hunt and Ashley, 1979)). Typically, the alteration rims contain more secondary minerals, such as goethite, ±ferrihydrite, ±phyllosilicate and hematite. This observation is consistent for both tephra, breccia and lava rocks (e.g. Table S3). Moreover, most of the samples show similar spectral reflectance for both the core and rim in the SWIR region (e.g. rh19 - Tawhainui lava flow, Iwikau Member, Whakapapa formation), indicating the overall fresh, young (≤50 ky) and unaltered state of the samples.

4.1.2. Supergene Argillic Alteration

These samples have additional spectral features to the unaltered lithologies, at around 650, 950, 1270, 1430, 1770, 2050, 2260, 2480 nm (e.g. rh10-11, rh21-23). These are consistent with Fe-oxides (e.g. goethite, hematite), with occasional jarosite and phyllosilicate phases, and are often limited to the alteration rim of the samples (Fig 3A). The alteration rims are often thicker than in the non-altered samples (>2 mm). The core is often comprised of fresh phenocrysts and micro-phenocryst populations characterized by sharp boundaries and sub- to euhedral crystals, lacking any pervasive alteration in the core of the samples (Figs 3C-D). This freshness of phenocrysts and micro-phenocrysts are also accompanied by magnetic susceptibilities, ranging from 0.005 to 0.02 SI (Miller et al., 2020b).

The spectroscopic data indicate the presence of both goethite (FeO(OH)) and hematite (Fe_2O_3) on Mt Ruapehu, with a dominance of goethite. The formation of such alteration minerals is strongly pH-dependent. Acidic (pH = 2–5) and alkaline conditions (pH = 10-14) favor the formation of goethite, while neutral pH promotes the formation of hematite (e.g. Schwertmann and Murad, 1983). However, both minerals can occur on the same hand specimen, indicating a highly heterogeneous occurrence of those minerals on a cm-scale.

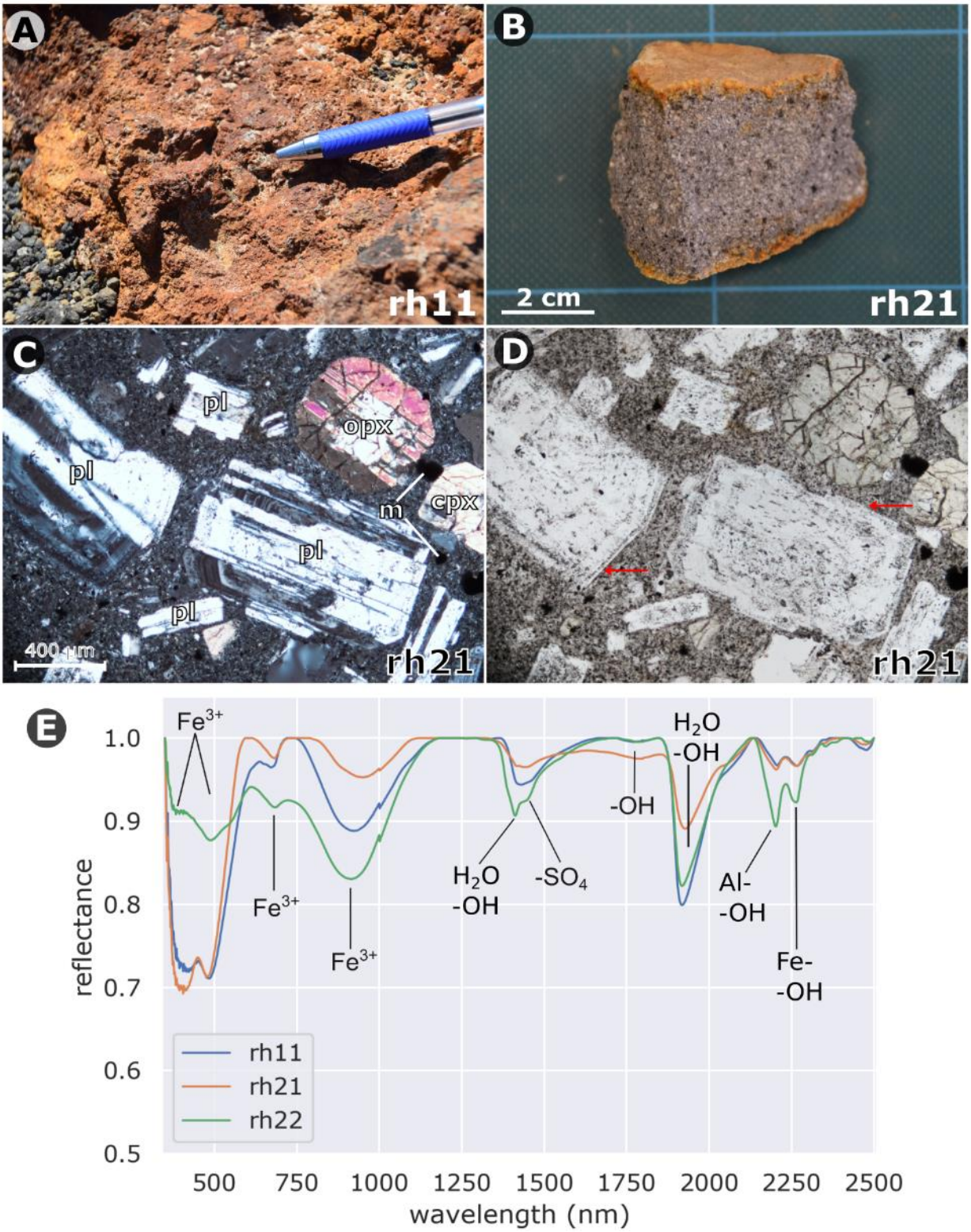

Figure 3. (A-B) Field and sample photos of the supergene argillic alteration showing various surface colorations and oxidations at outcrop scale. (C-D) Thin section photographs showing fresh phenocryst population with sharp contact (red arrow) viewed under cross-polarized light in

C and plane-polarized light in D. Abbreviations: plg – plagioclase, opx – orthopyroxene, cpx – clinopyroxene, m – magnetite. (E) Spectral reflectance profiles of representative samples showing supergene argillic alteration minerals.

Jarosite ($KFe_3(SO_4)_2(OH)_6$) is common in the alteration rims, suggesting a supergene origin as a weathering product of Fe-bearing rocks. It often forms from oxidation products under acidic conditions, and frequently forms in concert with ferric oxyhydroxides (Bishop and Murad, 2005). The jarosite phase (e.g. absorption feature at 2265 nm; Fig. 3E) is observed more often within the Te Herenga Formation (e.g. rh21-23) than in the Wahianoa Formations (e.g. rh10-11). This is consistent with the geochemistry of the original rocks (e.g. increased K and Fe content in the Te Herenga Formation; Table S1). The mineral assemblages are consistent with a paragenesis of a supergene argillic alteration and oxidation under atmospheric conditions, forming diverse alteration rims, depending on the primary rock geochemistry, and the exposure time to alteration processes (>50 ky). This process can be driven by metasomatism of K-bearing plagioclase phases by slightly acidic surface waters, causing surface weathering (e.g. Vasconcelos and Conroy, 2003).

4.1.3. Intermediate Argillic Alteration

This group is characterized by brownish to yellowish discoloration, with a partial to full replacement of the primary rock textures (Figs 4A-C), as well as the development of pervasive alteration rims with distinct spectral reflectance (Figs 4D-E). These rocks have absorption around 380, 435, 490, 960, 1420, 1780, 1915, 2205, 2290, 2315, 2390, 2480 nm with ±650, ±2240, ±1100 nm (rh3, rh12, rh26-rh34, rh36-41). The presence of absorption features at 380, 430 and 480 nm with occasional ~650 nm and ~940 nm are due to Fe^{3+} oxidation (Hunt and Ashley, 1979), indicating goethite as the main mineral phase with occasional jarosite, schwertmannite and pyrrhotite (Fig. 4E). These samples lack hematite, indicating formation under acidic conditions (Schwertmann and Murad, 1983). The SEM-EDS data further indicate that the groundmass of many alteration samples has disseminated subhedral pyrite with diameters between 5-30 μm (e.g. rh28, rh36, rh38, rh40, Figs 5A-D). Larger 300-500 μm, euhedral pyrite crystals are also present occasionally along grain boundaries, and within cavities and fractures (e.g. rh38; Fig. 5D). In addition to pyrite, Fe-rich, S-poor, occasionally Mn-rich, mineral phases have been identified, infilling cavity walls and fractures showing colloform, globular and botryoidal morphologies (Fig. 5A), is consistent with Fe-oxides (e.g. goethite), and Fe-sulfates [e.g. schwertmannite ($Fe_{16}O_{16}(SO_4)_{12\text{-}13}\cdot 10\text{-}12H_2O$)]. Jarosite occasionally appears as a pseudomorph after pyrite (e.g. rh36; Fig. 5C). The paragenesis of this phase is interpreted to be after supergene oxidation of the sulfide-rich host rock under strongly acidic conditions (e.g. Nordstrom, 1982). The SEM-EDS results show a higher volume% of pyrite in the Wahianoa than Te Herenga Formation. This can indicate time differences since those deposits are exposed to atmospheric conditions.

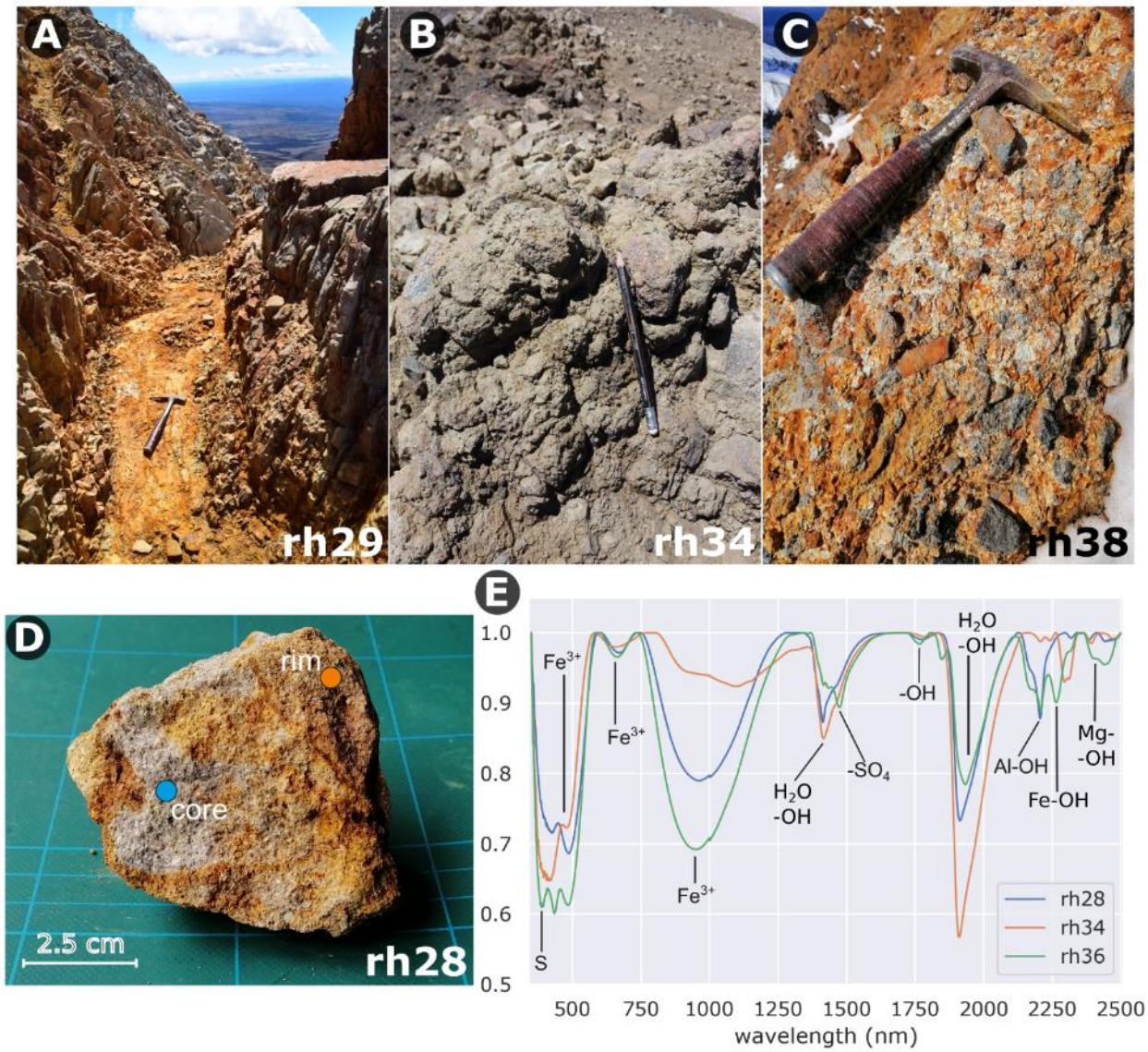

Figure 4. (A-C) Field photos of typical to intermediate argillic alteration on Mt Ruapehu. The samples are typically moderately to pervasively altered, showing various discoloration and clay mineral abundances. (D) Sample rh28 shows pervasive alteration preventing a clear distinction between crystal's rim and core. (E) Spectral reflectance profiles of representative samples. The spectral reflectance curves show absorption feature SWIR related to atomic vibration between Al-OH, Fe-OH and Mg-OH bonds, indicating the presence of phyllosilicates.

Based on SEM-EDS data, both primary plagioclase and pyroxene phases alter to amorphous Si-rich phases, consistent with various polymorphs of quartz. The alteration leaves abundant rim and core dissolution structures with well-developed microfractures, occasionally colloform and pseudomorph crystal habits within cavities (Fig. 5A). These are consistent with acid-induced mineral dissolution structures (e.g. Farquharson et al., 2019). Ti-magnetite phenocrysts and micro-phenocryst show commonly trellis-type lamellae textures, indicating leaching of the Fe and enrichment of Ti-oxides and silicates (e.g. rutile – $TiSO_2$, titanite – $CaTiSiO_5$), which is in

association with pyrite formation. This alteration process is responsible for the decrease of magnetic susceptibility of this group, which is between 0 and 0.01 SI (Miller et al., 2020b).

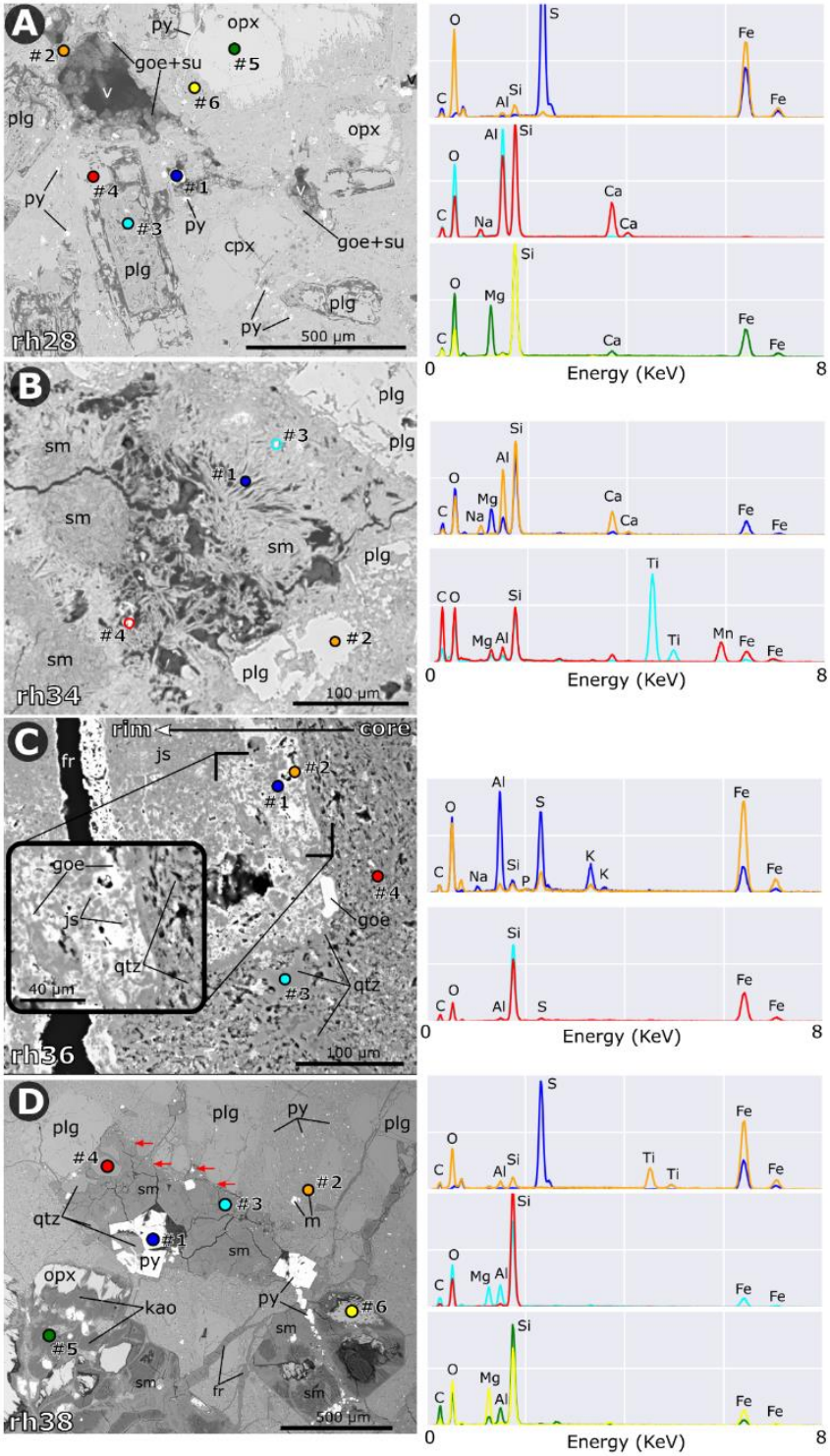

Figure 5. SEM (left column) and EDS (right column) results from the representative samples intermediate argillic alteration on Mt Ruapehu. The labelled EDS spots are color-coded. (A) rh28 shows typical phenocryst and micro-phenocrysts dissolution textures and extensive vug development with Fe-rich and S-poor infilling, comprising of Fe-oxides and Fe-hydroxy-sulfates. This sample is representative for the base of the Pinnacle Ridge. (B) rh34 shows vermiform, fibrous and tubular morphologies of smectite-group mineral, occupying fracture and vugs. (C) rh36 shows jarosite and goethite developed pseudomorphs after cubic pyrite. The groundmass is extensively replaced by silica (qtz). (D) rh38 shows well-developed cubic pyrite crystals co-occur with kaolin and smectite-group clay minerals (e.g. #5 and #6 on EDS) occupying vugs developed in former phenocrysts. A smaller population of pyrite occupies the interior walls of former phenocrysts, shown by red arrows. Abbreviations: v – void/vug, fr – fracture, plg – plagioclase, opx – orthopyroxene, cpx – clinopyroxene, m – titanomagnetite, sm – smectites, js – jarosite, kao – kaolinite, qtz – quartz, goe – goethite, su – Fe-sulfates, py – pyrite.

The absorption positions at 1420-1430, 1780, 2205, 2290, 2315, 2390 nm are consistent with the abundance of Na-Mg-Ca-Fe-rich phyllosilicates, including both kaolin and smectite group minerals. The distinction within phyllosilicates is challenging; however, reflectance spectroscopy in the VNIR and SWIR can detect vibrational and overtone-derived absorption features with hydrous minerals (Hunt and Ashley, 1979). This study used the shape, asymmetry and position of the absorption features to discriminate phyllosilicates and sulfates mostly in the SWIR (e.g. Table S2). Typically, samples with 1415 and 2205 nm (doublet) feature with inclination/asymmetry towards short-wavelength were interpreted as kaolin-group (e.g. kaolinite and halloysite - $Al_2(Si_2O_5)(OH)_4$). Absorption at 1415, 2205 nm and typically at 2290-2310 nm with inclination/asymmetry towards the long wavelength indicated the presence of the smectite group. The smectite group mineral were further discriminated by the position of their absorption feature at the SWIR region: montmorillonite $[(Na,Ca)_{0.33}(Al,Mg)_2(Si_4O_{10})(OH)_2\ nH_2O]$, nontronite $[(Na_{0.3}Fe_2((Si,Al)_4O_{10})(OH)_2\ nH_2O)]$, and vermiculite $[Mg_{0.7}(Mg,Fe,Al)_6(Si,Al)_8O_{20}(OH)_4\ 8H_2O]$.

The presence of phyllosilicates is often as fracture infilling minerals, showing thin crystallites with a vermiform, fibrous and tubular morphologies with hollow interiors, with Mg and Fe-enrichment (e.g. Fig. 5B). These textural and morphological features also indicate smectite group minerals (Beauchamps et al., 2019; Ece et al., 1999; Ta et al., 2017), indicating the dominance of montmorillonite and nontronite. Some samples (e.g. rh26) contains zeolite group minerals with acicular and radial crystal habits, occurring in fractures and cavity infilling.

Occasionally, euhedral to subhedral, hexagonal to prismatic, disseminated Cl-rich apatite crystals ($Ca_5(PO_4)_3Cl$) with diameters ranging from 30 to 50 μm, are embedded in phyllosilicate dominated fracture infills. Apatite is a minor, but ubiquitous mineral of plutonic and volcanic systems (Piccoli and Candela, 2002), and it is also present on Mt Ruapehu (Price et al., 2012). Constraining the paragenesis of this phase is problematic using spectroscopy, optical microscopy and SEM-EDS analysis, and it requires cathodoluminescence (Bouzari et al., 2016). The apatite found in rh34 contains a minor amount of S and Si, which can be incorporated into the apatite's crystal structure (e.g. Streck and Dilles, 1998), potentially indicating its magmatic origin.

Aluminum-Phosphate-Sulfate (APS) minerals occur in cavities as well-developed acicular crystals and are only observed in samples from the Wahianoa Formation. The SEM-EDS spectra show Ca-rich with minor peaks of Al and S, which might correspond to woodhouseite, $CaAl_3(PO_4,SO_4)(OH)_6$ (Dill, 2001; Stoffregen and Alpers, 1987). These APS minerals occasionally compliment acid-sulfate alteration in high-sulfidation epithermal systems which are

rich in Ca, P, Al, dissolved from primary apatite and plagioclase phases (Imura et al., 2019; Stoffregen and Alpers, 1987).

The mineral associations, their spectral, chemical and textural characteristics are all consistent with intermediate argillic alteration, formed in a highly acidic environment by hydrothermal fluids with temperatures between 150-250 °C (John et al., 2019; Simmons et al., 2005). This resulted in abundant pyrite as an oxidation product of the ascending H_2S-rich fluids below and around the paleo water table within the proto-Ruapehu edifice, within the Te Herenga and Wahianoa Formations. The pyrite-bearing rocks were then subject to supergene alteration after exposure to the atmospheric condition following flank collapses (Palmer and Neall, 1989; Tost et al., 2015) and erosion (e.g. glaciation and fluvial activity). This led to the formation of smectite-group minerals, such as montmorillonite and nontronite, and Fe-sulfates, potentially schwertmannite, both filling in fractures and vugs. Smectite group minerals often form after the initial oxidation of pyrite, producing acid water, followed by hydrolysis of feldspar and acid water buffering by the host rock, and colloidal deposition in open cavities and fractures at low-temperature (≤40 °C) (Fernández-Caliani et al., 2004). This paragenesis often produces minor barite ($BaSO_4$) phase (Fernández-Caliani et al., 2004), which has been identified as a minor phase in XRD (Mordensky et al., 2019a).

4.1.4. Advanced Argillic Alteration with minor silicification

Advanced argillic alteration occurs in vertical cliffs, and as reworked volcaniclastics deposits along the upper Whangaehu Valley, around the present-day Crater Lake area, and sampled as ballistic blocks from past eruptions (Figs 6A-C). These samples are often characterized by white, grey to pale yellow colors with abundance native sulfur, gypsum, amorphous silica precipitation and pyrite crystals with diameters up to 2 mm (Figs 6A-D). This group shows typical VNIR-SWIR absorption features around 380, 430, 480, 940, 1412, 1920, 2170, 2205, 2450 nm with ±390, ±1430, ±1475, ±1490, ±1783, ±2240, ±2260, ±2320, ±2400 nm (Fig. 6E). The spectral absorption position is consistent with goethite, phyllosilicates with the dominance of kaolin- group minerals over the smectite group, native sulfur, sulfates and sulfides. The SEM imagery shows completely dissolved phenocrysts and micro-phenocrysts of all primary minerals (e.g. Fig. 7A) The groundmass is often completely replaced by amorphous quartz (e.g. with localized silicification; Figs 6A and 7). Occasionally, samples show intense local silicification with complete to partial replacement of groundmass and phenocrysts, accompanied by minor sulfur and barite precipitation (e.g. blocks from the shore of the Crater Lake – rh52). The Ti-magnetite phases of the primary volcanic rocks have been completed altered, leaving Ti-rich residue and abundant pyrite crystals forming euhedral to subhedral on the outside of former magnetite crystals, and disseminated as a groundmass (Figs 7A and C). The destruction of magnetite produces very low magnetic susceptibility (e.g. 0 to 0.001 SI).

The groundmass occasionally has stockwork textures and colloform banding with vein and veinlets filled by native sulfur (e.g. rh44; Fig. 7B) and anhydrite (e.g. rh45; Fig. 7C). Anhydrite ($CaSO_4$) can be formed by progressive removal of acid anion species, such as SO_4, from the hydrothermal fluids, or by the exchange of aqueous H+ with cations in the host rock (Smith et al., 2017; Zimbelman et al., 2005). This paragenesis can also result in precipitation of kaolinite (Hynek et al., 2013). Samples exposed on the surface for an extended period were subject to depletion of their sulfur content (e.g. rh12) and hydration processes, forming gypsum, $CaSO_4 \cdot 2H_2O$ (e.g. rh48).

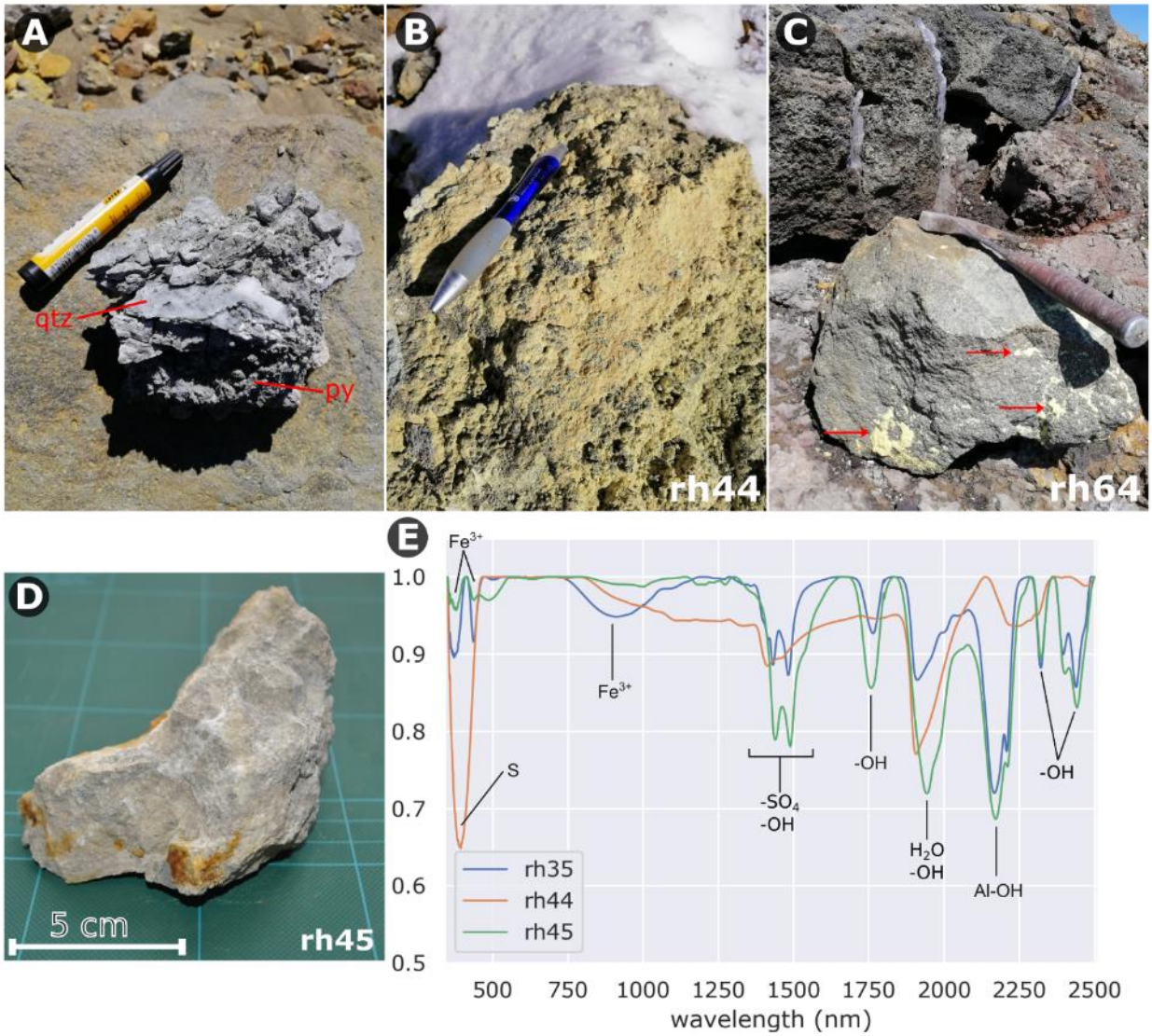

Figure 6. (A-D) Hand specimen samples of the advanced argillic alteration on Mt Ruapehu. The samples are often disintegrated, white to yellow in color, and show visible precipitation of pyrite/marcasite and native sulfur. (E) Spectral reflectance profiles of representative samples. The spectral reflectance curves show typical absorption features at around 1400-1500 nm which is associated with sulfates ($-SO_4$), while strong absorption due to Al-OH bonds and presence of crystalline water, indicating alunite and phyllosilicates (e.g. kaolin group minerals)

Besides anhydrite and gypsum, this group has alunite ($KAl_3(SO_4)_2(OH)_6$). Alunite exhibits spectral absorption features (e.g. Fig. 6E) due to the vibrations of hydroxyl (-OH) and metal-oxygen bonds (Al-OH) and lattice vibrations (Bishop and Murad, 2005). The alunite occurs on Mt Ruapehu as tabular crystals and as a constituent of the groundmass (Figs 7A and C). Both reflectance and SEM-EDS data indicate that alunite on Mt Ruapehu is not a pure endmember, but they show both K and Na enrichments. The origin of alunite is due to the oxidation of acidic fluids (e.g. H_2S) between the groundwater table and the surface (Zimbelman et al., 2005), or as supergene alteration of sulfides (Bladh, 1982). Currently, there is no active hydrothermal manifestation (e.g.

fumaroles, hot springs) besides the vent-hosted hydrothermal system beneath Crater Lake. The current Crater Lake and its hydrothermal system precipitate Na-alunite as oxidation of ascending H_2S hydrothermal fluids (Christenson and Wood, 1993). The formation of alunite within the Wahianoa Formation is interpreted to be formed under hypogene conditions due to its current stratigraphic position (e.g. exposed only at the lower parts of the Whangaehu valley). However, further isotope and radiometric dating are needed to confirm its relationship with the currently active hydrothermal system under the Crater Lake area.

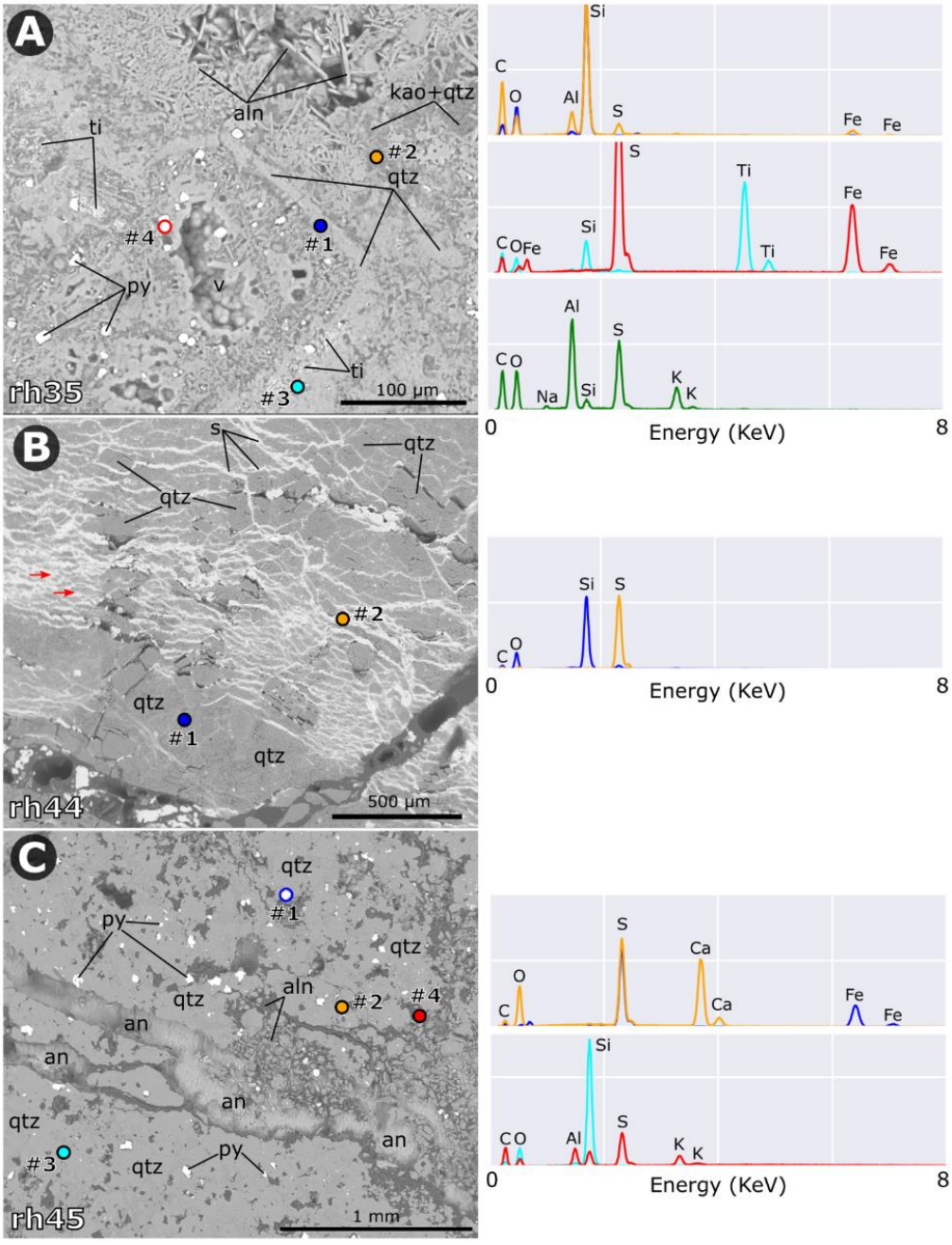

Figure 7. SEM (left column) and EDS (right column) results from the representative samples advanced argillic alteration on Mt Ruapehu. The labelled EDS spots are color coded. (A) rh35

shows tabular crystals of alunite, occurring together with kaolinite, pyrite and quartz. The groundmass and phenocryst are completely replaced by the alteration mineralogy; however, scattered Ti-rich phases are residues after the primary Ti-rich magnetite population (ti). (B) rh44 show extensive veinlets of precipitated native sulfur. (C) rh45 shows anhydrite filled fracture surrounded disseminated pyrite, alunite and quartz. Abbreviations: v – void/vug, kao – kaolinite, qtz – quartz, py – pyrite, al – alunite, s – sulfur, ti – Ti-rich phase.

The mineral associations are consistent with advanced argillic alteration (e.g. Sillitoe and Hedenquist, 2003) formed from a low pH of 1-4, hot hydrothermal fluids (120-300 °C), circulating within a magmatic-hydrothermal system (Boyce et al., 2007; John et al., 2019; John et al., 2008; Simmons et al., 2005; Swayze et al., 2014). However, the hydrothermal alteration can change on a small-scale between advanced argillic and intermediate argillic alteration styles.

4.2. Surface Mapping using Hyperspectral Imaging

The airborne hyperspectral image was used to create a hydrothermal alteration map of Mt Ruapehu through supervised image classification using a Random Forest algorithm (Fig. 8). The training process for the image classification was guided by the hydrothermal alteration mineralogy from SEM-EDS and spectroscopy analysis. The image classification accuracy using an independent validation population is 92.6%. Full retrieval of alteration classification on the surface is affected by the heavy cover of tephra, snow and ice on the surface of Mt Ruapehu (35.7% of the total area; Table 1) and the presence of shadows (Fig. 8A). The second largest unit mapped is the unaltered lava rocks (22.8 km^2). Supergene, intermediate and advanced argillic alteration have much smaller spatial extent on the surface, composing 4.8 km^2, 2.4 km^2 and 0.2 km^2 of the total area, respectively (Table 2). Accounting for the extensive surface cover, these hydrothermal alteration zones are expected to be minimum figures. The spectral average of the input training data shows distinct differences, including spectral features at 405, 493, 670 and 995 nm (goethite, hematite), 1160 nm (smectites), 1430-1495 nm (kaolinite, alunite, jarosite), 1763 nm (alunite), 2174 nm (alunite), 2200-2210 (Al-rich phyllosilicates), 2265 nm (jarosite), 2300-2390 nm (Fe- and Mg-rich phyllosilicates) (Fig. 9). These indicate that those minerals are critical to spectrally separate the mapped hydrothermal alteration types using airborne hyperspectral imagery.

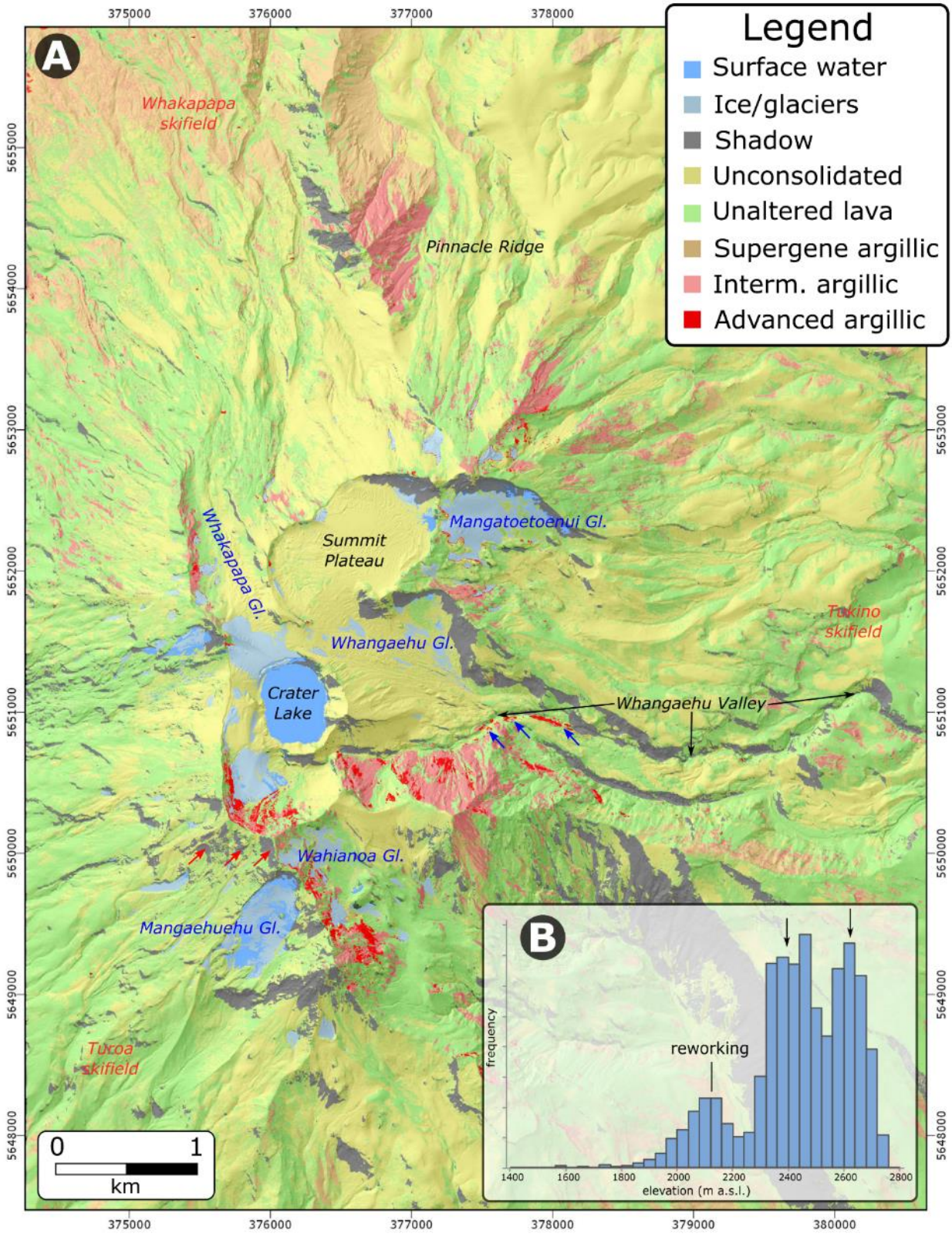

Figure 8. Hydrothermal alteration map of Mt Ruapehu based on the airborne hyperspectral imagery (A). The blue arrows show the location of the reworked deposits of the advanced argillic

alteration (e.g. samples rh44, rh45) along the Upper Whangaehu valley. Red arrows indicate areas with outcropping intermediate alteration (e.g. rh36), misclassified as shadow. The inset (B) shows the elevation histogram of the advanced argillic alteration rocks mapped by hyperspectral imaging, showing they occur predominantly at two distinct elevations (black arrows).

The error matrix shows numerous misclassifications between unconsolidated tephra and unaltered lava rocks (Table 1). This can be due to the similar chemical composition, resulting in similar reflectance profiles. Therefore, the spectral discrimination is most likely due to overall intensity of the reflected light, which, in turn, is a function of the grain size and illumination geometry (e.g. Clark and Roush, 1984). Another misclassification occurs between the supergene argillic and the intermediate argillic alteration types (Table 1). However, this misclassification occurred less frequently due to the presence of an absorption feature at 671 nm (e.g. goethite, ferrihydrite and hematite).

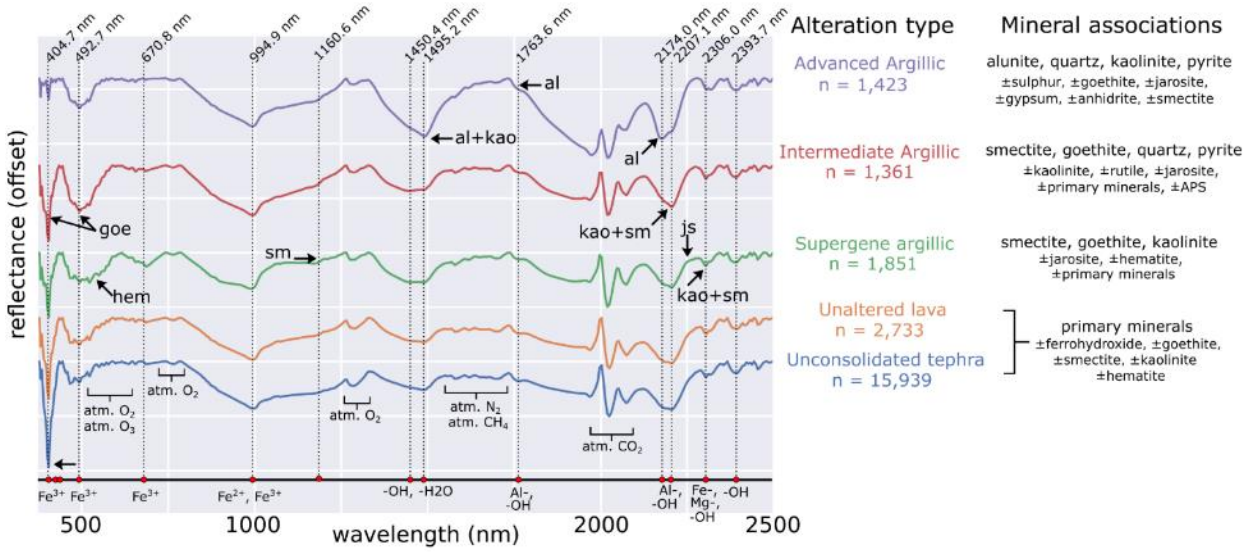

Figure 9: Continuum-removed spectral reflectance curves for the alteration classes on Mt Ruapehu, showing spectrally distinct absorption features of each class and the inferred mineralogy (black arrows) due to their unique mineralogy (right column). The graph also indicates the location of the atmospheric gasses, manifesting as noise in the hyperspectral data. The spectral curves are offset for clarity. Abbreviations: kao – kaolinite, al – alunite, sm – smectites, js – jarosite, goe – goethite, hem – hematite.

The most spectrally distinct class is the advanced argillic, due to its unique and pronounced absorption located at 2174 nm (alunite) and 2205 nm (kaolinite) (Fig. 9). The mapped occurrences correspond to three distinct elevation regions (Fig. 8B): (1) The lower occurrences correspond to the reworked deposits, along with the Whangaehu valley (blue arrows in Fig. 8A). The other two populations can indicate a spatial and temporal difference between the formation of advanced argillic suites (e.g. Wahianoa Formation versus the current Crater Lake hydrothermal system).

Table 1: Error matrix of the supervised image classification using the independent validation data (vertical columns) against the image classification results (horizontal rows). The values are pixel numbers. The highlighted values highlight the misclassifications.

		Image class								
Validation class	classes	water	ice	shade	tephra	unaltered lava	supergene argillic	intermediate argillic	advanced argillic	Total
	water	**3,381**	132	44	0	0	0	0	0	3,557
	ice	0	**1,952**	0	0	0	0	0	0	1,952
	shade	0	0	**5,820**	4	0	0	0	0	5,824
	tephra	2	0	0	**15,599**	699	9	3	18	16,330
	unaltered lava	5	0	0	1,094	**1,819**	77	69	0	3,064
	supergene argillic	0	0	0	47	26	**1,203**	42	0	1,318
	intermediate argillic	0	0	0	0	68	148	**727**	2	945
	advanced argillic	0	0	0	0	0	0	3	**595**	598
	Total	3,388	2,084	5,864	16,744	2,612	1,437	844	615	33,588

Table 2: Area statistics and image classification accuracy by image classes and hydrothermal alteration types on Mt Ruapehu.

Classes	**Alteration type/surface feature**	**User's Accuracy [%]**	**Producer's Accuracy [%]**	**Total area [pixel]**	**Total area [km^2]**
class 1	surface water	95.05	99.79	202,329	0.46
class 2	glaciers/snow	100	93.67	402,495	0.91
class 3	shadow	99.93	99.25	1,420,459	3.20
class 4	unconsolidated tephra	95.52	93.16	8,601,991	19.35
class 5	non-altered lava	59.37	69.64	10,158,097	22.86
class 6	supergene argillic alteration	91.27	83.72	2,125,567	4.78
class 7	intermediate argillic alteration	76.93	86.14	1,075,363	2.42
class 8	advanced argillic alteration	99.5	96.75	93,699	0.21

4.3. Subsurface Mapping using Aeromagnetic Data

The 3D depth of hydrothermal alteration can be mapped using aeromagnetic data and subsequent inversion models (Finn et al., 2018; Finn et al., 2001; Miller et al., 2020b), if the lack of the magnetic susceptibility is due to hydrothermal alteration which dissolves (Ti-) magnetite crystals. Based on the SEM imaging, there is a systematic dissolution of (Ti-) magnetite with increasingly pervasive hydrothermal alteration (Fig 10). Therefore the magnetic susceptibility measurements and the inversion model of Mt Ruapehu (Miller et al., 2020b) indicates the hydrothermal alteration, which can be used to link surface alteration patterns from the hyperspectral image classification (Figs 10D and 11). However, identifying low magnetic susceptibility caused by hydrothermal alteration is complicated by the variable amounts of magnetite content and its Ti-impurity in the host rock (Fig. 10D), meaning that some fresh, low magnetite content andesites can have similar magnetic susceptibility to supergene alteration. Intermediate and advanced argillic alteration deposits tend to have, however, generally lower magnetic susceptibility (e.g. ≤0.01 SI; Fig 10D).

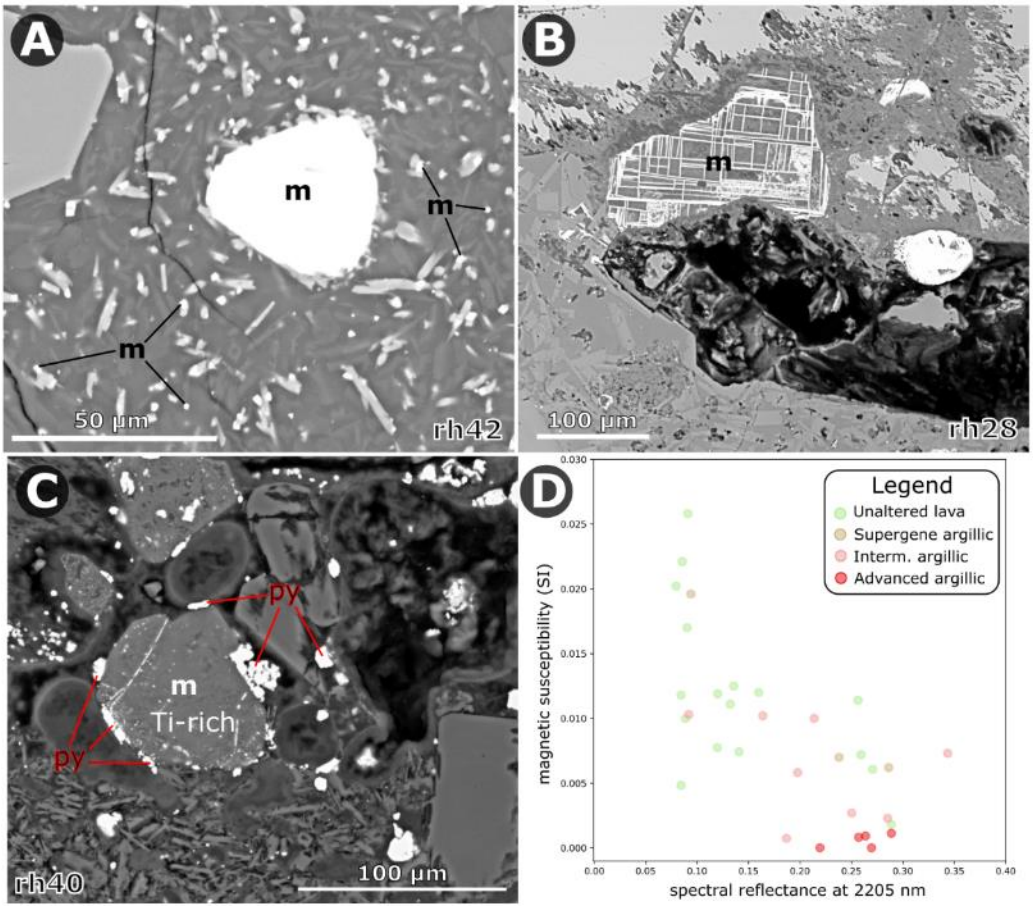

Figure 10. Titanomagnetite dissolution textures as a function of hydrothermal alteration types: (A) non-altered, (B) intermediate with well-developed trellis structures, and (C) advanced argillic alterations. (D) The graph shows the relationship between measured magnetic susceptibility values (SI) and spectral reflectance at 2205 nm.

The largest region of hydrothermally altered rocks is located within the Pinnacle Ridge on the southeastern flanks and to a moderate extent beneath the entire Summit Plateau. The cross-cutting dykes exposed at the Te Herenga Formation show higher magnetic susceptibility compared to the lavas of the Wahianoa Formation, possibly due to the larger grain size of the intruded rocks. The low to moderate levels of magnetic susceptibility (e.g. Turoa side; Fig. 11) are due to volcaniclastic deposits, mixed with glacial sediments and thin intercalated lava flows (Conway et al., 2016; Townsend et al., 2017), which some of might also be hydrothermally altered (Miller et al., 2020b). The demagnetized zones beneath Summit Plateau are patchy (Fig. 11B), in agreement with electrical resistivity highs observed in the magnetotelluric model, which suggest the dominance of chlorite (Jones et al., 2008). The geophysical model linked with alteration mineralogy and surface alteration distribution from the hyperspectral imaging indicates that the hydrothermal alteration interpreted in the aeromagnetic model mostly corresponds to intermediate argillic alteration. Intermediate argillic alteration is rich in smectite-group minerals, which can explain the observed the high electrical resistivity zone beneath the northern part of the Summit Plateau [e.g. “R1” anomaly in Jones et al. (2008)]. Moreover, this alteration type has a wide range of magnetic susceptibilities (0.001 to 0.01 SI) (e.g. Fig. 10D), contributing to the patch-work patterns in the aeromagnetic data (Miller et al., 2020b).

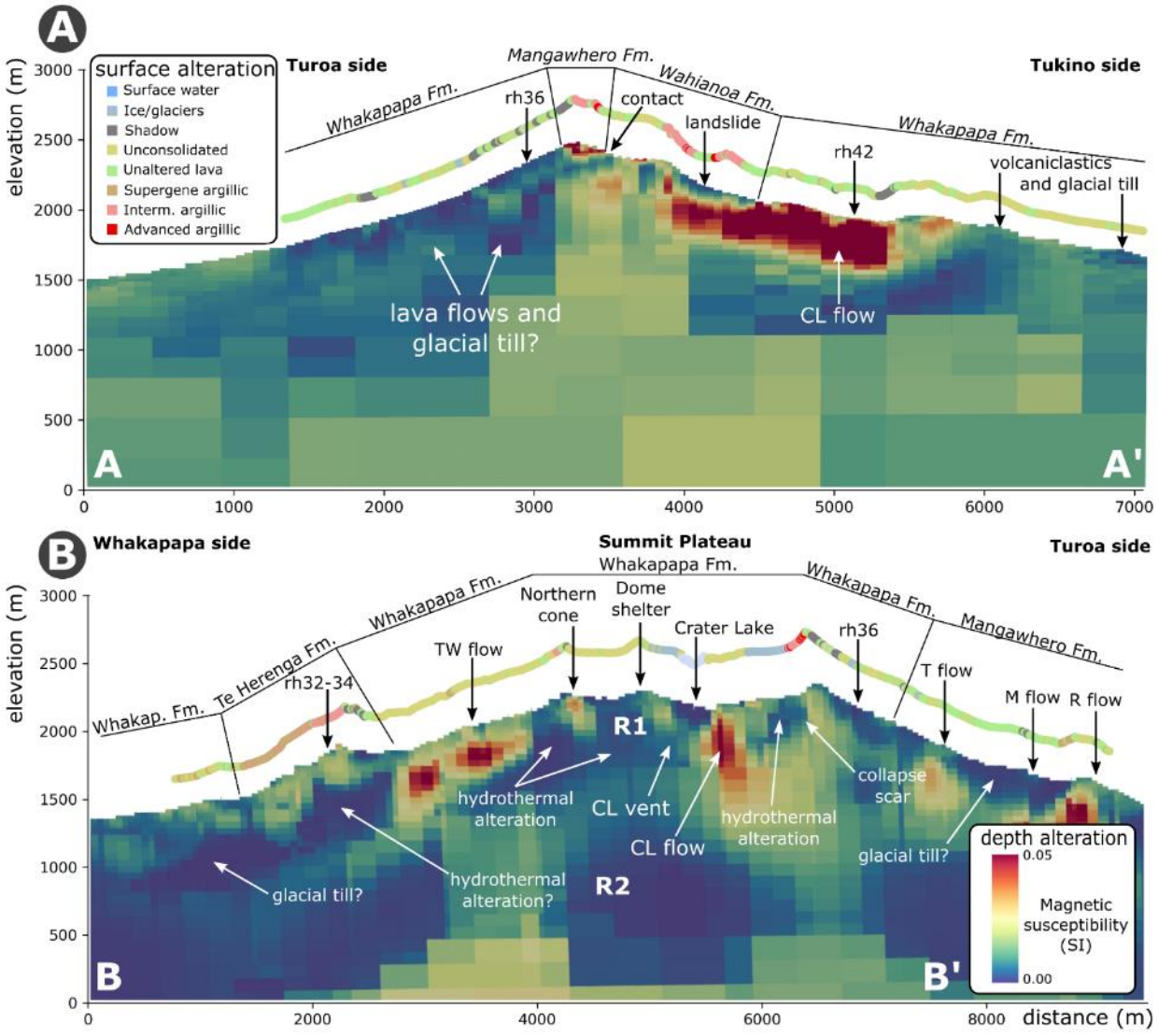

Figure 11. Cross-section through the magnetic susceptibility model of Mt Ruapehu along the A-A' and B-B' profiles from Fig. 1. On (B), R1 and R2 correspond to the electric resistivity highs from Jones et al. (2008). The dots above the topography show the hydrothermal alteration types mapped on the surface using hyperspectral imaging. The colors correspond to Fig. 11, and the profiles are offset by 200 m for clarity. Abbreviations: CL vent – Crater Lake vent; CL flow - Crater Lake Member lava of Whakapapa Formation (5-y); TW flow - Iwikau Member of Whakapapa Formation - Tawhainui flows (6 ky); T flow - Turoa Member of Whakapapa Formation (15-12 ky); M Flow - Mangaehuehu Member of Mangawhero Formation (45-42 ky); R flow - Rangataua Member lava of Whakapapa Formation (10-15 ky).

5. Discussion

5.1. Integration of Hyperspectral Imaging with Airborne Geophysics

Airborne hyperspectral remote sensing can identify hydrothermal alteration minerals, and through image classification, a hydrothermal alteration map can be created. The hydrothermal alteration map only represents surface alteration, which can be heavily hampered by the surface cover (e.g. tephra, glacial till, alluvium and colluvium accumulation). However, the distribution of the hydrothermal alteration can still be reconstructed with the aid of ancillary field data through microscopic petrographical and mineralogical information. Hyperspectral imaging provides a versatile framework for hydrothermal alteration mapping, which correlates well with the magnetic susceptibility model of Mt Ruapehu (e.g. Fig. 11). Conversely, the inversion of aeromagnetic data can indicate spatial distribution of subsurface alteration at depth, but it provides no information on the style of hydrothermal alteration, and interpretation of moderate alteration can be misled by unaltered rocks with similar magnetic susceptibility. Furthermore, aeromagnetic data is also insensitive to rock water saturation that is a key determinant in slope stability (Finn et al., 2018; Miller et al., 2020a). Thus, limitations in both hyperspectral remote sensing and geophysical data can be overcome by integrating both methods, allowing a comprehensive assessment of both surface and subsurface alteration patterns.

The paragenesis of hydrothermal alteration types and volumes of the altered rock masses provide a great conceptual model for volcanic hydrothermal systems, vastly improving our understanding of volcanic evolution and associated natural hazards. Specifically, at Mt Ruapehu, since the hydrothermal alteration is only exposed along ridge tops and on steep slopes off of these ridges because of tephra cover, the extent of hydrothermal alteration is seemingly minor on the surface. However, geophysical data (e.g. aeromagnetic) suggests a much larger extent is altered. This is likely the case at similar long-lived volcanoes worldwide. This calls for the need to integrate remote sensing and geophysical datasets for developing new volcano assessment tools to monitor and map shallow hydrothermal alteration within composite volcanoes.

Further direction to utilize hyperspectral remote sensing for hydrothermal alteration mapping can include mapping of individual mineral species through spectral feature matching (Clark et al., 2003), or wavelength mapping (van der Meer et al., 2018). Moreover, alteration minerals often occur as an intimate granular mixture, requiring spectral unmixing algorithms (Roberts et al., 1998), or using regression approaches with synthetically mixed training data (Okujeni et al., 2013). These research directions will need dedicated studies in the future.

5.2. The Role of Mineral Imprinting

The weathering and hydrothermal alteration on Mt Ruapehu has produced diverse mineral suites, some of which can be formed through multiple paragenesis including supergene modification through oxidation of sulfides, such as pyrite exposed to groundwater or surface water (Fig. 12A). These processes cause changes to meta-stable hydrothermal alteration minerals, leading to “imprinting”, complicating the reconstruction of hydrothermal alteration history on long-lived composite volcanoes. For example, supergene oxidation can form jarosite (in Fe-rich low pH conditions), alunite (in moderate pH and Al-rich conditions), as well as hydroxy-sulfate and oxyhydroxide minerals (Bishop and Murad, 2005; Schwertmann and Murad, 1983; Zolotov and Shock, 2005), which cannot be discriminated by spectroscopic techniques and hyperspectral remote sensing. Mt Ruapehu has abundant Fe-oxides, mostly goethite, which can be formed from both oxidation processes of primary mineral phases rich in Fe (e.g. titano-magnetite, clino- and orthopyroxenes) and oxidation and breakdown of hydrothermal pyrite (Brady et al., 1986; Noack et al., 1993). The abundance of goethite, and its confinement to higher flanks, can also be attributed

to the extensive glacial history of Mt Ruapehu. The chemical weathering occurring beneath glaciers is primarily driven by microorganic activity, thriving on meltwater solution rich in oxidized pyrite, silica and anions, such as SO_4^{2-} (Mitchell et al., 2013; Rutledge et al., 2018).

The integration of field sampling, hyperspectral and aeromagnetic data have, however, allowed us to constrain the spatial distribution of inactive and currently active hydrothermal systems, allowing discrimination of mineral imprinting processes on Mt Ruapehu (Fig. 12B). These correspond to the oldest Te Herenga Formation, outcropping at the Pinnacle Ridge (Fig. 1, 8), in which the intrusion-related hydrothermal system lead to acid sulfate alteration, causing primary mineralogy to be altered to pyrite, phyllosilicates, quartz-dominated alteration minerals, superimposed with extensive smectite formation due to prolong surface oxidation of pyrite (Fig. 12B). This leads to distinct vertical and stratigraphic changes in a sulfide-to-clay ratio within the altered rocks. Areas <2000 m a.s.l. show less extensive oxidation of pyrite (e.g. rh28) than the elevated, >2100 m a.s.l parts of the Pinnacle Ridge (rh32-34). This can be explained by the delay in surface erosion and thus the exposure of the sulfides to atmospheric O_2, leading to enrichment of smectites.

The second oldest part of Mt Ruapehu is the Wahianoa Formation that hosts extensive areas of intermediate argillic alteration (Fig. 12B). The alteration mineralogy and textures (e.g. sharp boundaries of the pyrite crystals) are better preserved than within the Te Herenga Formation, indicating much shorter exposure to atmospheric conditions. This observation is in line with the geological history of the upper Whangaehu valley (Fig. 1 and 8), which developed after the Mangaio flank collapse 4.6 ky ago (Donoghue and Neall, 2001). Furthermore, the Wahianoa Formation also hosts advanced argillic alteration (e.g. alunite, pyrite, quartz and phyllosilicates). This can originate from (1) surface oxidation of pyrite, (2) within the magmatic-hydrothermal system that existed during the Wahianoa Formation time, or (3) a steam-heated overprinting alteration due to the proximity of the currently active Crater Lake hydrothermal systems by condensation of magmatic vapor into the later outflow of groundwater (Fig. 12B). In (2) and (3), the alunite formed directly due to the ascent-driven oxidation of H_2S-rich fluids and wall-rock interactions. Alunite, however, occurs with anhydrite on Mt Ruapehu, which is more consistent with the paragenesis of (2). The distribution of alunite bearing rocks, therefore, can indicate the position of the paleo water table within the Wahianoa eruptive center between 80-50 ky ago. The lowest levels of in-situ alunite occurrence on Mt Ruapehu is at 2250 m a.s.l. This elevation is just slightly higher than the maximum elevation of the Pinnacle Ridge (2237 m a.s.l.), potentially indicating the role of erosion on the exposure of alunite-bearing rocks.

5.3. A Model for Hydrothermal Alteration

Aeromagnetic data observes that Mt Ruapehu currently has an active but spatially confined vent-hosted hydrothermal system (Christenson and Wood, 1993). This is in sharp contrast with the neighboring Tongariro Volcanic Complex, in which has abundant hydrothermal surface manifestation, including fumaroles and hot pools (Miller et al., 2018; Moore and Brock, 1981). This observation is in line with the hyperspectral image-derived hydrothermal alteration map, which does not indicate pervasive hydrothermal alteration across the summit area. While there is limited surface hydrothermal alteration on Mt Ruapehu (i.e. intermediate and advanced argillic styles), covering 2.6 km^2 or only 5% of the total area (Fig. 8), the location of this alteration is scattered throughout the mapped areas. This indicates a complex spatial-temporal evolution of

hydrothermal activity at Mt Ruapehu that reflects discrete development stages over the last 200 ky (Fig. 12).

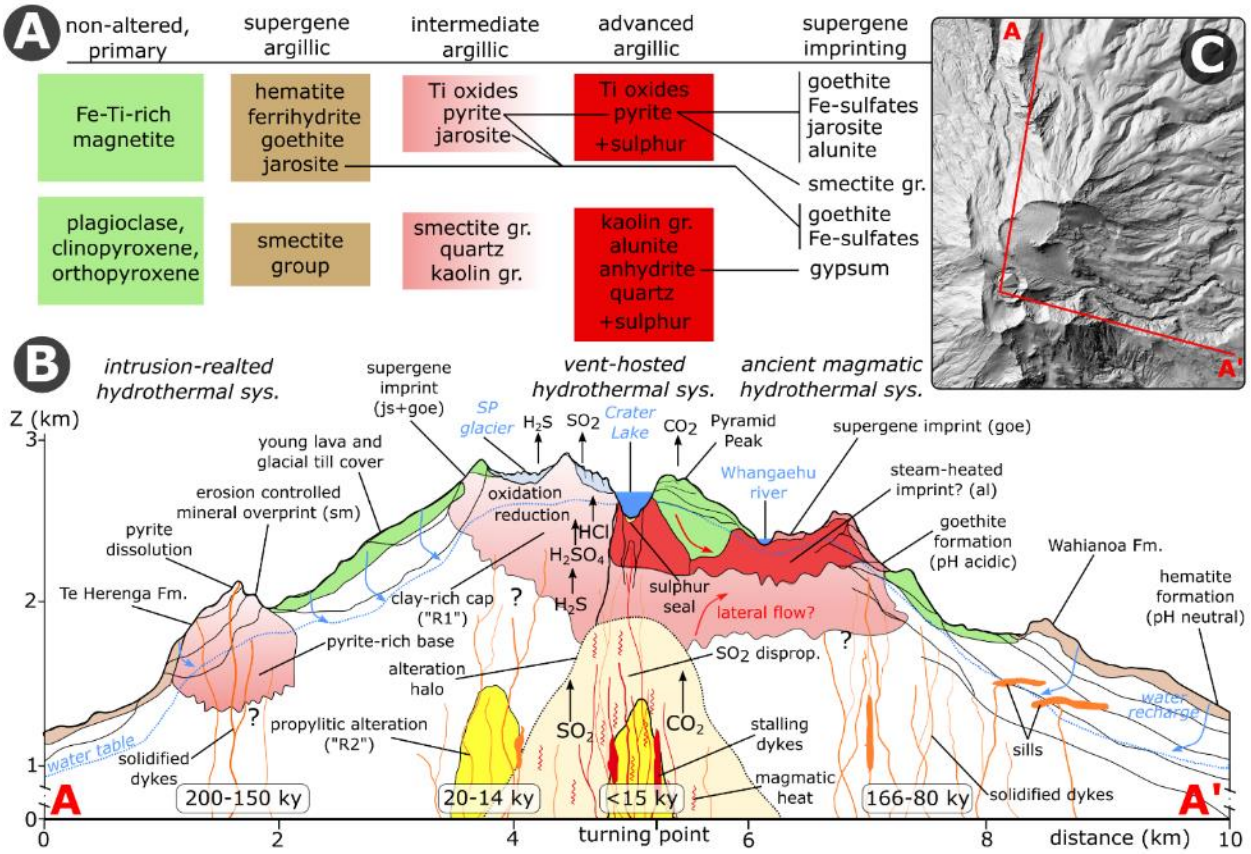

Figure 12. A model for surface weathering and hydrothermal alteration on Mt Ruapehu volcano. (A) Hydrothermal alteration sequence of typical primary minerals (green), and their supergene argillic (light brown), intermediate (light pink) and advanced (red), their supergene imprinting mineral associations. (B) The distribution of hydrothermal alteration types and the main hydrothermal features on Mt Ruapehu along the A-A' profile line in (C). Abbreviations: SP glacier – Summit Plateau glacier.

At Mt Ruapehu, the source of the magmatic heat and gasses are located at depths between 2 and 9 km as a network of stalling and crystallizing dykes, forming a melt-rich crystal mush inferred from volatile content and major element chemistry of groundmass glass and phenocryst-hosted melt inclusions (e.g. Kilgour et al., 2013). This zone has also been imaged as a resistivity anomaly in magnetotelluric (Ingham et al., 2009) and seismic tomography surveys (Rowlands et al., 2005). This network of magma releases magmatic gasses (e.g. H_2O, CO_2 and SO_2; Fig. 12B), which after disproportionation can form acidic hydrothermal fluids dominated by H_2S, and precipitate native sulfur (Christenson et al., 2010; Mavrogenes and Blundy, 2017). This type of hydrothermal fluid promotes acid sulfate wall-rock alteration within the volcanic edifice above the magmatic heat source (Rye et al., 1992; Zimbelman et al., 2005). The low pH hydrothermal fluids then induce wall-rock alteration at depth underneath the currently active Crater Lake. A similar ancient

hydrothermal system has been imaged by magnetotelluric surveys beneath the northern Summit Plateau as a vertically elongated high resistivity zone, which can correspond to a chlorite-rich altered zone (Jones et al., 2008). Chlorite is a typical indicator mineral of propylitic alteration (Neal et al., 2018). A broader region around this zone also appears to be demagnetized (e.g. Fig. 12B; Miller et al., 2020b), which can correspond to the development of an enlarged alteration halo (Fig. 12B).

Propylitic alteration often grades vertically into intermediate argillic alteration (e.g. John et al., 2019), which outcrops only sporadically around the Summit Plateau, as indicated by the hyperspectral remote sensing data (Fig 8). This type of alteration occurs as the ascending H_2S-rich hydrothermal fluids react with the andesitic host rock's ferrous minerals (e.g. titano-magnetite) to form sulfides, such as pyrite, under reducing conditions (e.g. rh38, rh40, rh28, rh33; Fig. 12A), as observed similarly at Mt Rainer, USA (John et al., 2008). This leads to the formation of disseminated pyrite crystals. On Mt Ruapehu, well-developed, cubic pyrite crystals are typical, indicating hydrothermal fluid supersaturation conditions and higher formation temperatures of ~250 °C (e.g. Murowchick and Barnes, 1987). The dissolution of Ti-magnetite population is also responsible for demagnetization of the host rock, making it possible to detect hydrothermal alteration using aeromagnetic techniques (e.g. Fig. 11B; Miller et al., 2020b). This zone has also been mapped as a higher-resistivity zone on magnetotelluric data (e.g. R1 in Fig. 13B; Jones et al., 2008), indicating the dominance of intermediate argillic alteration beneath the entire Summit Plateau (Fig. 12B). This area corresponds to the relict hydrothermal system of the Paretetaitonga and Tureiti cones, active between 20 and 12 ky ago (Townsend et al., 2017). Besides the precipitation of pyrite, and enrichment of Ti, the wall-rock alteration on Mt Ruapehu also leads to K and partial Na and Ca depletions, and Si, Al, Fe, Mg and O enrichments, along with the formation of kaolin and smectite group minerals (Fig. 12A).

At locations of intense hydrothermal fluid circulation, the intermediate argillic alteration transitions into advanced argillic alteration, characterized by the abundance of sulfate minerals (e.g. alunite), and localized zones of silicification (e.g. vuggy texture). Sulfates (e.g. alunite, anhydrite and barite) often form around or above the water table within a hydrothermal system due to oxidation of the ascending H_2S-rich fluids (Fig. 12B) (Rye, 2005; Zimbelman et al., 2005). These are limited to areas directly beneath the Crater Lake and within the Wahianoa Formation (Fig.12B). The origin of sulfate precipitation within the Wahianoa Formation can be either (1) associated with the magmatic-hydrothermal system developed during the Wahianoa Formation, or (2) formed as a steam-heated alteration on the margin of the currently active Crater Lake hydrothermal systems due to lateral flow of groundwater (Fig. 12B). The origin can be further investigated using stable isotope geochemistry and K-Ar radiometric dating on the K-phase within the alunite.

5.4. Volcanic Hazard Implications

The influence of alteration on physical and mechanical rock properties depends on rock type, initial microstructural and physical properties of the rock, nature of the hydrothermal fluid, and duration of rock-fluid interaction, resulting in varying processes of mineral dissolution, replacement, and/or precipitation (Heap et al., 2020 and references therein). This study described the production of kaolin and smectite phyllosilicate clay minerals as a result of acid-sulfate alteration. The main consequences of the formation of these clay minerals are the replacement of strong rock by a weaker, clay-rich rock, precipitation of clay into pores and microfractures, and

the deposition of clay along bedding structures or at the interface between volcanic deposits (Heap et al., 2019; Watters et al., 1995). The degree/intensity of clay alteration combined with the degree of saturation has been shown to alter overall strength, density, and elasticity of volcanic rock (Mordensky et al., 2019a; Siratovich et al., 2016; Watters et al., 1995; Wyering et al., 2014). Experimental observations have also shown that an increase in alteration increases the propensity for pore collapse or ductile failure behavior (Mordensky et al., 2019a; Siratovich et al., 2016), which decreases porosity and permeability as the material is deformed and pores are compacted (e.g. Farquharson et al., 2017). This, in turn, has implications for pore fluid pressure, magma degassing, and eruption characteristics (Cassidy et al., 2018; Heap et al., 2019; Okumura and Sasaki, 2014). For example, a reduction in permeability from clay precipitation into pores and fractures can prevent the migration of hydrothermal fluids or magma degassing, leading to increased pore pressures that can decrease material strength (leading to collapse events) and increase the likelihood of phreatic eruptions (e.g. Day, 1996). The presence of clays can also reduce the effective pressure required for ductile behavior, resulting in an anomalously shallow ductile zone that may prevent brittle fracturing and thus volcano-tectonic seismicity prior to some volcanic eruptions (Mordensky et al., 2019a).

A thorough investigation of the type and distribution of alteration is required to highlight potential source areas for collapse and mass flows events (e.g. debris avalanches and landslides). The existence of a single vent-hosted hydrothermal system at Mt. Ruapehu suggests that current (ongoing) hydrothermal alteration may be limited to the active summit crater and conduit (Fig. 11B). However, spectroscopy and aeromagnetic data suggest an abundance of alteration exists in the upper parts of the south and southeast flanks, either due to lateral fluid migration and/or older/inactive hydrothermal systems. The mineralogical, hyperspectral and geophysical data all indicate widespread hydrothermal altered rocks underneath the Summit Plateau, which is likely to be due to intermediate argillic alteration (Fig. 14B). This alteration is abundant in smectite group minerals that can precipitate into pores and fractures, thus decreasing rock permeability and preventing the migration of hydrothermal fluids beneath the Summit Plateau. The reconstructed mineral suites and hydrothermal alteration map can be combined with ongoing rock mechanical studies at Mt Ruapehu to provide an improved understanding of the geomechanical properties and rock mass behavior. This, combined with volume estimates of altered bodies from aeromagnetic data (Miller et al., 2020b), is vital information for both defining the probability of failures initiating from these areas and implementing new numerical simulations of mass flows from composite volcanoes.

6. Summary and Conclusions

The present study integrates alteration mineralogy with hyperspectral imaging and aeromagnetic data inversion to provide a conceptual model for hydrothermal alteration. These geophysical and geochemical techniques can also essential to map the 3D distribution of altered rock masses on composite volcanoes. However, the methods used in this study separately would not be able to fully describe the hydrothermal alteration. A combined approach is therefore promoted here to better understand such complex geosystems. This is particularly important for composite volcanoes with long-lived and nested eruptive centres, which can leave behind relict hydrothermal systems, potentially invisible on the surface.

Hyperspectral imaging is extremely effective at delineating surface hydrothermal alteration through image classification techniques, allowing quantitative recognition of hydrothermal

alteration minerals. Furthermore, airborne imaging system allows very high-resolution imagery to be acquired, benefitting a detailed spatial mapping of hydrothermal alteration styles due to their unique combination of mineralogy. However, this technology currently is not capable of assessing deep-seated hydrothermal alteration and was limited by unconsolidated tephra, snow and ice cover, and shadow.

Aeromagnetic inversion models can complement airborne hyperspectral imaging to quantify subsurface hydrothermal alteration, by mapping the volume of demagnetized rocks. Hence, the combination of the airborne remote sensing and geophysical approaches allows the creation of a detailed, three-dimensional conceptual model for supergene weathering and hydrothermal alteration processes over the last 200 ky at the Mt Ruapehu volcano.

Water saturation can be an important driven for pore pressure fluctuation in volcanic aquifers. It cannot be detected by aeromagnetic surveys, nor with hyperspectral remote sensing. A useful add-on can be for future studies to combined those survey techniques above with electrical and electromagnetic geophysical methods, such as Direct-Current resistivity, induced polarization and airborne electromagnetics for including groundwater levels water saturation. These methods need to be included in current monitoring methods to improve our understanding of the trigger mechanism of slope failures.

The detailed surface and subsurface imaging data provide here versatile and high-resolution baseline information for future studies, which is critical to assess future volcanic activity and spatial/temporal changes on frequently active volcanoes. The methods used herein can be extended to other composite volcanoes worldwide. Results from these studies, in combination with mechanical information on rock-strength, can be applied to identify the volume and configuration of structurally weak material. Better identification and delineation of flank instability hazards, obtained through the application of the alteration models, can be used to improve hazard assessment and mitigation efforts around active volcanoes.

7. Acknowledgement

This study was supported by Natural Hazards Research Platform ("Too big to fail? – A multidisciplinary approach to predict collapse and debris flow hazards from Mt. Ruapehu"). C.A.M is also supported by the Ministry of Business, Innovation and Employment-funded GNS Science Volcanic Hazards Program The authors are grateful for Specim Ltd. for support on image processing. Field assistance from Abbey Douglas, Marija Voloschina, Soós Ildikó, Ermanno Brosch, Cecilia Rodriguez-Gomez, Charline Lormand, Boglarka Nemeth, Tyler Barton, Angela Denes, Emily Koot and Istvan Hajdu is much appreciated. The authors are grateful for the Department of Conservation, and Iwi around the Tongariro National Park for providing sampling permits (Authorization Number: 63618-GEO), as well as the Tukino Alpine Sports Club for help with ground access. Thank you to Michael Rosenberg for sharing XRD data and providing samples of the ballistic blocks from the 95/96 Ruapehu eruption.

The airborne hyperspectral image is publicly available at: 10.5281/zenodo.3905352

The aeromagnetic data is publicly available at https://figshare.com/articles/Data_and_python_script/11289149

8. References

Abdallah, S., Utsugi, M., Aizawa, K., Uyeshima, M., Kanda, W., Koyama, T., and Shiotani, T. (2020). Three-dimensional electrical resistivity structure of the Kuju volcanic group, Central Kyushu, Japan

revealed by magnetotelluric survey data. *Journal of Volcanology and Geothermal Research, 400*, 106898. http://www.sciencedirect.com/science/article/pii/S0377027319305414

Ball, J. L., Calder, E. S., Hubbard, B. E., and Bernstein, M. L. (2013). An assessment of hydrothermal alteration in the Santiaguito lava dome complex, Guatemala: implications for dome collapse hazards. *Bulletin of Volcanology, 75*(1), 676. https://doi.org/10.1007/s00445-012-0676-z

Ball, J. L., Taron, J., Reid, M. E., Hurwitz, S., Finn, C., and Bedrosian, P. (2018). Combining Multiphase Groundwater Flow and Slope Stability Models to Assess Stratovolcano Flank Collapse in the Cascade Range. *Journal of Geophysical Research: Solid Earth, 123*(4), 2787-2805. https://agupubs.onlinelibrary.wiley.com/doi/abs/10.1002/2017JB015156

Beauchamps, G., Ledésert, B., Hébert, R., Navelot, V., and Favier, A. (2019). The characterisation of an exhumed high-temperature paleo-geothermal system on Terre-de-Haut Island (the Les Saintes archipelago, Guadeloupe) in terms of clay minerals and petrophysics. *Geothermal Energy, 7*(1), 6. journal article. https://doi.org/10.1186/s40517-019-0122-y

Belgiu, M., and Drăguţ, L. (2016). Random forest in remote sensing: A review of applications and future directions. *ISPRS Journal of Photogrammetry and Remote Sensing, 114*, 24-31. http://www.sciencedirect.com/science/article/pii/S0924271616000265

Berlo, K., van Hinsberg, V., Suparjan, Purwanto, B. H., and Gunawan, H. (2020). Using the composition of fluid seepage from the magmatic-hydrothermal system of Kawah Ijen volcano, Indonesia, as a monitoring tool. *Journal of Volcanology and Geothermal Research, 399*, 106899. http://www.sciencedirect.com/science/article/pii/S0377027319306353

Bishop, J., L.,, and Murad, E. (2005). The visible and infrared spectral properties of jarosite and alunite. In *American Mineralogist* (Vol. 90, pp. 1100).

Bladh, K. W. (1982). The formation of goethite, jarosite, and alunite during the weathering of sulfide-bearing felsic rocks. *Economic Geology, 77*(1), 176-184. https://doi.org/10.2113/gsecongeo.77.1.176

Bouzari, F., Hart, C. J. R., Bissig, T., and Barker, S. (2016). Hydrothermal Alteration Revealed by Apatite Luminescence and Chemistry: A Potential Indicator Mineral for Exploring Covered Porphyry Copper Deposits. *Economic Geology, 111*(6), 1397-1410. https://doi.org/10.2113/econgeo.111.6.1397

Bowles-Martinez, E., and Schultz, A. (2020). Composition of Magma and Characteristics of the Hydrothermal System of Newberry Volcano, Oregon, From Magnetotellurics. *Geochemistry, Geophysics, Geosystems, 21*(3), e2019GC008831. https://agupubs.onlinelibrary.wiley.com/doi/abs/10.1029/2019GC008831

Boyce, A. J., Fulignati, P., Sbrana, A., and Fallick, A. E. (2007). Fluids in early stage hydrothermal alteration of high-sulfidation epithermal systems: A view from the Vulcano active hydrothermal system (Aeolian Island, Italy). *Journal of Volcanology and Geothermal Research, 166*(2), 76-90. http://www.sciencedirect.com/science/article/pii/S0377027307002181

Brady, K. S., Bigham, J. M., Jaynes, W. F., and Logan, T. J. (1986). Influence of Sulfate on Fe-Oxide Formation: Comparisons with a Stream Receiving Acid Mine Drainage. *Clays and Clay Minerals, 34*(3), 266-274. https://doi.org/10.1346/CCMN.1986.0340306

Breiman, L. (2001). Random Forests. *Machine Learning, 45*(1), 5-32. journal article. http://dx.doi.org/10.1023/A:1010933404324

Buddington, A. F., and Lindsley, D. H. (1964). Iron-Titanium Oxide Minerals and Synthetic Equivalents. *Journal of Petrology, 5*(2), 310-357. https://doi.org/10.1093/petrology/5.2.310

Capra, L. (2006). Abrupt climatic changes as triggering mechanisms of massive volcanic collapses. *Journal of Volcanology and Geothermal Research, 155*(3), 329-333. http://www.sciencedirect.com/science/article/pii/S0377027306001855

1014 Carrino, T. A., Crósta, A. P., Toledo, C. L. B., and Silva, A. M. (2018). Hyperspectral remote sensing
1015 applied to mineral exploration in southern Peru: A multiple data integration approach in the
1016 Chapi Chiara gold prospect. *International Journal of Applied Earth Observation and*
1017 *Geoinformation, 64*, 287-300.
1018 http://www.sciencedirect.com/science/article/pii/S0303243417301071
1019 Cassidy, M., Manga, M., Cashman, K., and Bachmann, O. (2018). Controls on explosive-effusive volcanic
1020 eruption styles. *Nature Communications, 9*(1), 2839. https://doi.org/10.1038/s41467-018-
1021 05293-3
1022 Christenson, B. W. (2000). Geochemistry of fluids associated with the 1995–1996 eruption of Mt.
1023 Ruapehu, New Zealand: signatures and processes in the magmatic-hydrothermal system. *Journal*
1024 *of Volcanology and Geothermal Research, 97*(1), 1-30.
1025 http://www.sciencedirect.com/science/article/pii/S0377027399001675
1026 Christenson, B. W., Reyes, A. G., Young, R., Moebis, A., Sherburn, S., Cole-Baker, J., and Britten, K.
1027 (2010). Cyclic processes and factors leading to phreatic eruption events: Insights from the 25
1028 September 2007 eruption through Ruapehu Crater Lake, New Zealand. *Journal of Volcanology*
1029 *and Geothermal Research, 191*(1), 15-32.
1030 http://www.sciencedirect.com/science/article/pii/S0377027310000223
1031 Christenson, B. W., and Wood, C. P. (1993). Evolution of a vent-hosted hydrothermal system beneath
1032 Ruapehu Crater Lake, New Zealand. *Bulletin of Volcanology, 55*(8), 547-565. journal article.
1033 https://doi.org/10.1007/BF00301808
1034 Clark, R. N., Gallagher, A. J., and Swayze, G. A. (1990). Material absorption band depth mapping of
1035 imaging spectrometer data using the complete band shape least-squares algorithm
1036 simultaneously fit to multiple spectral features from multiple materials. *Proceedings of the Third*
1037 *Airborne Visible/Infrared Imaging Spectrometer (AVIRIS) Workshop, JPL Publication 90-54*, 176-
1038 186.
1039 Clark, R. N., and Roush, T. L. (1984). Reflectance spectroscopy: Quantitative analysis techniques for
1040 remote sensing applications. *Journal of Geophysical Research: Solid Earth, 89*(B7), 6329-6340.
1041 https://agupubs.onlinelibrary.wiley.com/doi/abs/10.1029/JB089iB07p06329
1042 Clark, R. N., Swayze, G. A., Livo, K. E., Kokaly, R. F., Sutley, S. J., Dalton, J. B., et al. (2003). Imaging
1043 spectroscopy: Earth and planetary remote sensing with the USGS Tetracorder and expert
1044 systems. *Journal of Geophysical Research E: Planets, 108*(12), 1-44.
1045 http://pubs.er.usgs.gov/publication/70025059
1046 Cockett, R., Kang, S., Heagy, L. J., Pidlisecky, A., and Oldenburg, D. W. (2015). SimPEG: An open source
1047 framework for simulation and gradient based parameter estimation in geophysical applications.
1048 *Computers & Geosciences, 85*, 142-154.
1049 http://www.sciencedirect.com/science/article/pii/S009830041530056X
1050 Collard, N., Peiffer, L., and Taran, Y. (2020). Heat and fluid flow dynamics of a stratovolcano: The Tacaná
1051 Volcanic Complex, Mexico-Guatemala. *Journal of Volcanology and Geothermal Research, 400*,
1052 106916. http://www.sciencedirect.com/science/article/pii/S0377027320300652
1053 Conway, C. E., Gamble, J. A., Wilson, C. J. N., Leonard, G. S., Townsend, D. B., and Calvert, A. T. (2018).
1054 New petrological, geochemical, and geochronological perspectives on andesite-dacite magma
1055 genesis at Ruapehu volcano, New Zealand. *American Mineralogist, 103*(4), 565-581.
1056 https://doi.org/10.2138/am-2018-6199
1057 Conway, C. E., Leonard, G. S., Townsend, D. B., Calvert, A. T., Wilson, C. J. N., Gamble, J. A., and Eaves, S.
1058 R. (2016). A high-resolution 40Ar/39Ar lava chronology and edifice construction history for
1059 Ruapehu volcano, New Zealand. *Journal of Volcanology and Geothermal Research, 327*, 152-179.
1060 http://www.sciencedirect.com/science/article/pii/S0377027316302062

Cronin, S. J., Neall, V. E., Lecointre, J. A., and Palmer, A. S. (1997). Changes in Whangaehu river lahar characteristics during the 1995 eruption sequence, Ruapehu volcano, New Zealand. *Journal of Volcanology and Geothermal Research, 76*(1), 47-61. http://www.sciencedirect.com/science/article/pii/S0377027396000649

Crosta, A. P., Sabine, C., and Taranik, J. V. (1998). Hydrothermal Alteration Mapping at Bodie, California, using AVIRIS Hyperspectral Data. *Remote Sensing of Environment, 65*(3), 309–319.

Crowley, J. K., Hubbard, B. E., and Mars, J. C. (2003). Analysis of potential debris flow source areas on Mount Shasta, California, by using airborne and satellite remote sensing data. *Remote Sensing of Environment, 87*(2–3), 345-358. //www.sciencedirect.com/science/article/pii/S0034425703001925

Day, S. J. (1996). Hydrothermal pore fluid pressure and the stability of porous, permeable volcanoes. *Geological Society, London, Special Publications, 110*(1), 77-93. https://sp.lyellcollection.org/content/specpubgsl/110/1/77.full.pdf

del Potro, R., and Hürlimann, M. (2009). The decrease in the shear strength of volcanic materials with argillic hydrothermal alteration, insights from the summit region of Teide stratovolcano, Tenerife. *Engineering Geology, 104*(1), 135-143. http://www.sciencedirect.com/science/article/pii/S0013795208002457

Dill, H. G. (2001). The geology of aluminium phosphates and sulphates of the alunite group minerals: a review. *Earth-Science Reviews, 53*(1), 35-93. http://www.sciencedirect.com/science/article/pii/S0012825200000350

Dill, H. G. (2016). Kaolin: Soil, rock and ore: From the mineral to the magmatic, sedimentary and metamorphic environments. *Earth-Science Reviews, 161*, 16-129. http://www.sciencedirect.com/science/article/pii/S0012825216301568

Donoghue, S. L., and Neall, V. E. (1996). Tephrostratigraphic studies at Tongariro Volcanic Centre, New Zealand: An overview. *Quaternary International, 34–36*(0), 13-20. http://www.sciencedirect.com/science/article/pii/1040618295000658

Donoghue, S. L., and Neall, V. E. (2001). Late Quaternary constructional history of the southeastern Ruapehu ring plain, New Zealand. *New Zealand Journal of Geology and Geophysics, 44*(3), 439-466. https://doi.org/10.1080/00288306.2001.9514949

Ece, Ö. I., Çoban, F., Güngör, N., and Suner, F. (1999). Clay Mineralogy and Occurrence of Ferrian Smectites Between Serpentinite Saprolites and Basalts in Biga Peninsula, Northwest Turkey. *Clays and Clay Minerals, 47*(3), 241-251. journal article. https://doi.org/10.1346/CCMN.1999.0470301

Farquharson, J. I., Baud, P., and Heap, M. J. (2017). Inelastic compaction and permeability evolution in volcanic rock. *Solid Earth, 8*(2), 561-581. https://se.copernicus.org/articles/8/561/2017/

Farquharson, J. I., Wild, B., Kushnir, A. R. L., Heap, M. J., Baud, P., and Kennedy, B. (2019). Acid-Induced Dissolution of Andesite: Evolution of Permeability and Strength. *Journal of Geophysical Research: Solid Earth, 124*(1), 257-273. https://agupubs.onlinelibrary.wiley.com/doi/abs/10.1029/2018JB016130

Fernández-Caliani, J. C., Crespo, E., Rodas, M., Barrenechea, J. F., and Luque, F. J. (2004). Formation of Nontronite from Oxidative Dissolution of Pyrite Disseminated in Precambrian Felsic Metavolcanics of the Southern Iberian Massif (Spain). *Clays and Clay Minerals, 52*(1), 106-114. https://doi.org/10.1346/CCMN.2004.0520110

Fernández-Caliani, J. C., Crespo, E., Rodas, M., Barrenechea, J. F., and Luque, F. J. (2004). Formation of nontronite from oxidative dissolution of pyrite disseminated in precambrian felsic metavolcanics of the southern Iberian Massif (Spain). *Clays and Clay Minerals, 52*(1), 106-114. https://doi.org/10.1346/CCMN.2004.0520110

1108 Finn, C. A., Deszcz-Pan, M., Ball, J. L., Bloss, B. J., and Minsley, B. J. (2018). Three-dimensional
1109 geophysical mapping of shallow water saturated altered rocks at Mount Baker, Washington:
1110 Implications for slope stability. *Journal of Volcanology and Geothermal Research, 357*, 261-275.
1111 http://www.sciencedirect.com/science/article/pii/S0377027317307199
1112 Finn, C. A., Sisson, T. W., and Deszcz-Pan, M. (2001). Aerogeophysical measurements of collapse-prone
1113 hydrothermally altered zones at Mount Rainier volcano. *Nature, 409*(6820), 600-603.
1114 10.1038/35054533. http://dx.doi.org/10.1038/35054533
1115 Fournier, D., Heagy, L. J., and Oldenburg, D. W. (2020). Sparse magnetic vector inversion in spherical
1116 coordinates. *Geophysics, 85*(3), J33-J49. https://library.seg.org/doi/abs/10.1190/geo2019-
1117 0244.1
1118 Galvão, L. S., Almeida-Filho, R., and Vitorello, Í. (2005). Spectral discrimination of hydrothermally altered
1119 materials using ASTER short-wave infrared bands: Evaluation in a tropical savannah
1120 environment. *International Journal of Applied Earth Observation and Geoinformation, 7*(2), 107-
1121 114. http://www.sciencedirect.com/science/article/pii/S0303243405000310
1122 Gamble, J. A., Price, R. C., Smith, I. E. M., McIntosh, W. C., and Dunbar, N. W. (2003). 40Ar/39Ar
1123 geochronology of magmatic activity, magma flux and hazards at Ruapehu volcano, Taupo
1124 Volcanic Zone, New Zealand. *Journal of Volcanology and Geothermal Research, 120*(3-4), 271-
1125 287. Article. https://www.scopus.com/inward/record.uri?eid=2-s2.0-
1126 0037303551&partnerID=40&md5=8c7c5f379bf6d40a9c3ac02f1552839e
1127 Gamble, J. A., Wood, C. P., Price, R. C., Smith, I. E. M., Stewart, R. B., and Waight, T. (1999). A fifty year
1128 perspective of magmatic evolution on Ruapehu Volcano, New Zealand: verification of open
1129 system behaviour in an arc volcano. *Earth and Planetary Science Letters, 170*(3), 301-314.
1130 http://www.sciencedirect.com/science/article/pii/S0012821X99001065
1131 Ganino, C., Libourel, G., and Bernard, A. (2019). Fumarolic incrustations at Kudryavy volcano
1132 (Kamchatka) as a guideline for high-temperature (>850 °C) extinct hydrothermal systems.
1133 *Journal of Volcanology and Geothermal Research, 376*, 75-85.
1134 http://www.sciencedirect.com/science/article/pii/S0377027319300058
1135 Graham, I. J., and Hackett, W. R. (1987). Petrology of Calc-alkaline Lavas from Ruapehu Volcano and
1136 Related Vents, Taupo Volcanic Zone, New Zealand. *Journal of Petrology, 28*(3), 531-567.
1137 https://doi.org/10.1093/petrology/28.3.531
1138 Gresse, M., Vandemeulebrouck, J., Byrdina, S., Chiodini, G., Roux, P., Rinaldi, A. P., et al. (2018).
1139 Anatomy of a fumarolic system inferred from a multiphysics approach. *Scientific Reports, 8*(1),
1140 7580. https://doi.org/10.1038/s41598-018-25448-y
1141 Hackett, W. R., and Houghton, B. F. (1989). A facies model for a quaternary andesitic composite volcano:
1142 Ruapehu, New Zealand. *Bulletin of Volcanology, 51*(1), 51-68. journal article.
1143 http://dx.doi.org/10.1007/BF01086761
1144 Heap, M. J., Gravley, D. M., Kennedy, B. M., Gilg, H. A., Bertolett, E., and Barker, S. L. L. (2020).
1145 Quantifying the role of hydrothermal alteration in creating geothermal and epithermal mineral
1146 resources: The Ohakuri ignimbrite (Taupō Volcanic Zone, New Zealand). *Journal of Volcanology*
1147 *and Geothermal Research, 390*, 106703.
1148 http://www.sciencedirect.com/science/article/pii/S0377027319304688
1149 Heap, M. J., Kennedy, B. M., Pernin, N., Jacquemard, L., Baud, P., Farquharson, J. I., et al. (2015).
1150 Mechanical behaviour and failure modes in the Whakaari (White Island volcano) hydrothermal
1151 system, New Zealand. *Journal of Volcanology and Geothermal Research, 295*, 26-42. Article.
1152 https://www.scopus.com/inward/record.uri?eid=2-s2.0-
1153 84924873678&doi=10.1016%2fj.jvolgeores.2015.02.012&partnerID=40&md5=703e2dab063ab2
1154 643eee69f8ab7d0d9d

Heap, M. J., Troll, V. R., Kushnir, A. R. L., Gilg, H. A., Collinson, A. S. D., Deegan, F. M., et al. (2019). Hydrothermal alteration of andesitic lava domes can lead to explosive volcanic behaviour. *Nature Communications, 10*(1), 5063. https://doi.org/10.1038/s41467-019-13102-8

Hellman, M. J., and Ramsey, M. S. (2004). Analysis of hot springs and associated deposits in Yellowstone National Park using ASTER and AVIRIS remote sensing. *Journal of Volcanology and Geothermal Research, 135*(1–2), 195-219. http://www.sciencedirect.com/science/article/pii/S037702730400037X

Hunt, G. R., and Ashley, R. P. (1979). Spectra of altered rocks in the visible and near infrared. *Economic Geology, 74*(7), 1613-1629. https://doi.org/10.2113/gsecongeo.74.7.1613

Hynek, B. M., McCollom, T. M., Marcucci, E. C., Brugman, K., and Rogers, K. L. (2013). Assessment of environmental controls on acid-sulfate alteration at active volcanoes in Nicaragua: Applications to relic hydrothermal systems on Mars. *Journal of Geophysical Research: Planets, 118*(10), 2083-2104. https://agupubs.onlinelibrary.wiley.com/doi/abs/10.1002/jgre.20140

Imura, T., Minami, Y., Ohba, T., Matsumoto, A., Arribas, A., and Nakagawa, M. (2019). Hydrothermal Aluminum-Phosphate-Sulfates in Ash from the 2014 Hydrothermal Eruption at Ontake Volcano, Central Honshu, Japan. *Minerals, 9*(8), 462. https://www.mdpi.com/2075-163X/9/8/462

Ingham, M. R., Bibby, H. M., Heise, W., Jones, K. A., Cairns, P., Dravitzki, S., et al. (2009). A magnetotelluric study of Mount Ruapehu volcano, New Zealand. *Geophysical Journal International, 179*(2), 887-904. https://onlinelibrary.wiley.com/doi/abs/10.1111/j.1365-246X.2009.04317.x

Inostroza, M., Aguilera, F., Menzies, A., Layana, S., González, C., Ureta, G., et al. (2020). Deposition of metals and metalloids in the fumarolic fields of Guallatiri and Lastarria volcanoes, northern Chile. *Journal of Volcanology and Geothermal Research, 393*, 106803. http://www.sciencedirect.com/science/article/pii/S0377027319304536

James, M. R., and Robson, S. (2012). Straightforward reconstruction of 3D surfaces and topography with a camera: Accuracy and geoscience application. *Journal of Geophysical Research: Earth Surface, 117*(F3), 1-17. http://dx.doi.org/10.1029/2011JF002289

John, D. A., Lee, R. G., Breit, G. N., Dilles, J. H., Calvert, A. T., Muffler, L. J. P., and Clynne, M. A. (2019). Pleistocene hydrothermal activity on Brokeoff volcano and in the Maidu volcanic center, Lassen Peak area, northeast California: Evolution of magmatic-hydrothermal systems on stratovolcanoes. *Geosphere, 15*(3), 946-982. https://doi.org/10.1130/GES02049.1

John, D. A., Sisson, T. W., Breit, G. N., Rye, R. O., and Vallance, J. W. (2008). Characteristics, extent and origin of hydrothermal alteration at Mount Rainier Volcano, Cascades Arc, USA: Implications for debris-flow hazards and mineral deposits. *Journal of Volcanology and Geothermal Research, 175*(3), 289-314. http://www.sciencedirect.com/science/article/pii/S0377027308001200

Johnston, D. M., Houghton, B. F., Neall, V. E., Ronan, K. R., and Paton, D. (2000). Impacts of the 1945 and 1995–1996 Ruapehu eruptions, New Zealand: An example of increasing societal vulnerability. *Geological Society of America Bulletin, 112*(5), 720-726. http://gsabulletin.gsapubs.org/content/112/5/720.abstract

Jones, K. A., Ingham, M. R., and Bibby, H. M. (2008). The hydrothermal vent system of Mount Ruapehu, New Zealand — a high frequency MT survey of the summit plateau. *Journal of Volcanology and Geothermal Research, 176*(4), 591-600. http://www.sciencedirect.com/science/article/pii/S0377027308002643

Kereszturi, G., Schaefer, L. N., Schleiffarth, W. K., Procter, J., Pullanagari, R. R., Mead, S., and Kennedy, B. (2018). Integrating airborne hyperspectral imagery and LiDAR for volcano mapping and monitoring through image classification. *International Journal of Applied Earth Observation and Geoinformation, 73*, 323-339. http://www.sciencedirect.com/science/article/pii/S0303243418305300

Kilgour, G., Blundy, J., Cashman, K., and Mader, H. M. (2013). Small volume andesite magmas and melt–mush interactions at Ruapehu, New Zealand: evidence from melt inclusions. *Contributions to Mineralogy and Petrology, 166*(2), 371-392. https://doi.org/10.1007/s00410-013-0880-7

Kokaly, R. F., Clark, R. N., Swayze, G. A., Livo, K. E., Hoefen, T. M., Pearson, N. C., et al. (2017). *USGS Spectral Library Version 7* (1035). Retrieved from Reston, VA: http://pubs.er.usgs.gov/publication/ds1035

Kruse, F. A., Baugh, W. M., and Perry, S. L. (2015). Validation of DigitalGlobe WorldView-3 Earth imaging satellite shortwave infrared bands for mineral mapping. *Journal of Applied Remote Sensing, 9*(1), 1-17.

Le Gonidec, Y., Rosas-Carbajal, M., Bremond d'Ars, J. d., Carlus, B., Ianigro, J. C., Kergosien, B., et al. (2019). Abrupt changes of hydrothermal activity in a lava dome detected by combined seismic and muon monitoring. *Scientific Reports, 9*(1), 3079. https://doi.org/10.1038/s41598-019-39606-3

Liu, C., Frazier, P., and Kumar, L. (2007). Comparative assessment of the measures of thematic classification accuracy. *Remote Sensing of Environment, 107*(4), 606-616. http://www.sciencedirect.com/science/article/pii/S0034425706004068

López, D. L., and Williams, S. N. (1993). Catastrophic Volcanic Collapse: Relation to Hydrothermal Processes. *Science, 260*(5115), 1794-1796. https://science.sciencemag.org/content/sci/260/5115/1794.full.pdf

Matsunaga, Y., Kanda, W., Takakura, S., Koyama, T., Saito, Z., Seki, K., et al. (2020). Magmatic hydrothermal system inferred from the resistivity structure of Kusatsu-Shirane Volcano. *Journal of Volcanology and Geothermal Research, 390*, 106742. http://www.sciencedirect.com/science/article/pii/S0377027319303312

Mavrogenes, J., and Blundy, J. (2017). Crustal sequestration of magmatic sulfur dioxide. *Geology, 45*(3), 211-214. https://doi.org/10.1130/G38555.1

Mayer, K., Scheu, B., Yilmaz, T. I., Montanaro, C., Albert Gilg, H., Rott, S., et al. (2017). Phreatic activity and hydrothermal alteration in the Valley of Desolation, Dominica, Lesser Antilles. *Bulletin of Volcanology, 79*(12), 82. https://doi.org/10.1007/s00445-017-1166-0

Mia, B., and Fujimitsu, Y. (2012). Mapping hydrothermal altered mineral deposits using Landsat 7 ETM+ image in and around Kuju volcano, Kyushu, Japan. *Journal of Earth System Science, 121*(4), 1049-1057. https://doi.org/10.1007/s12040-012-0211-9

Miller, C. A., Christenson, B. W., Byrdina, S., Vandemeulebrouck, J., Brakenrig, T., Britten, K., et al. (2020a). Snapshot of a magmatic/hydrothermal system from electrical resistivity tomography and fumarolic composition, Whakaari/White Island, New Zealand. *Journal of Volcanology and Geothermal Research, 400*, 106909. http://www.sciencedirect.com/science/article/pii/S0377027320301529

Miller, C. A., Kang, S. G., Fournier, D., and Hill, G. (2018). Distribution of Vapor and Condensate in a Hydrothermal System: Insights From Self-Potential Inversion at Mount Tongariro, New Zealand. *Geophysical Research Letters, 45*(16), 8190-8198. https://agupubs.onlinelibrary.wiley.com/doi/abs/10.1029/2018GL078780

Miller, C. A., Schaefer, L. N., Kereszturi, G., and Fournier, D. (2020b). Three-Dimensional Mapping of Mt. Ruapehu Volcano, New Zealand, From Aeromagnetic Data Inversion and Hyperspectral Imaging. *Journal of Geophysical Research: Solid Earth, 125*(2), e2019JB018247. https://doi.org/10.1029/2019JB018247

Miller, C. A., and Williams-Jones, G. (2016). Internal structure and volcanic hazard potential of Mt Tongariro, New Zealand, from 3D gravity and magnetic models. *Journal of Volcanology and Geothermal Research, 319*, 12-28. //www.sciencedirect.com/science/article/pii/S0377027316300245

Mitchell, A. C., Lafrenière, M. J., Skidmore, M. L., and Boyd, E. S. (2013). Influence of bedrock mineral composition on microbial diversity in a subglacial environment. *Geology, 41*(8), 855-858. https://doi.org/10.1130/G34194.1

Moore, P. R., and Brock, J. L. (1981). A physical and chemical survey of Ketetahi Hot Springs, Mt Tongariro, New Zealand. *New Zealand Journal of Science, 24*(2), 161-177.

Mordensky, S. P., Heap, M. J., Kennedy, B. M., Gilg, H. A., Villeneuve, M. C., Farquharson, J. I., and Gravley, D. M. (2019a). Influence of alteration on the mechanical behaviour and failure mode of andesite: implications for shallow seismicity and volcano monitoring. *Bulletin of Volcanology, 81*(8), 44. journal article. https://doi.org/10.1007/s00445-019-1306-9

Mordensky, S. P., Kennedy, B. M., Villeneuve, M. C., Lavallée, Y., Reichow, M. K., Wallace, P. A., et al. (2019b). Increasing the Permeability of Hydrothermally Altered Andesite by Transitory Heating. *Geochemistry, Geophysics, Geosystems, 20*(11), 5251-5269. https://agupubs.onlinelibrary.wiley.com/doi/abs/10.1029/2019GC008409

Murowchick, J. B., and Barnes, H. L. (1987). Effects of temperature and degree of supersaturation on pyrite morphology. *American Mineralogist, 72*(11-12), 1241-1250.

Murphy, R. J., Taylor, Z., Schneider, S., and Nieto, J. (2015). Mapping clay minerals in an open-pit mine using hyperspectral and LiDAR data. *European Journal of Remote Sensing, 48*(1), 511-526. https://doi.org/10.5721/EuJRS20154829

Nakagawa, M., Wada, K., Thordarson, T., Wood, C. P., and Gamble, J. A. (1999). Petrologic investigations of the 1995 and 1996 eruptions of Ruapehu volcano, New Zealand: formation of discrete and small magma pockets and their intermittent discharge. *Bulletin of Volcanology, 61*(1), 15-31. https://doi.org/10.1007/s004450050259

Neal, L. C., Wilkinson, J. J., Mason, P. J., and Chang, Z. (2018). Spectral characteristics of propylitic alteration minerals as a vectoring tool for porphyry copper deposits. *Journal of Geochemical Exploration, 184*, 179-198. http://www.sciencedirect.com/science/article/pii/S0375674216303958

Noack, Y., Colin, F., Nahon, D., Delvigne, J., and Michaux, L. (1993). Secondary-mineral formation during natural weathering of pyroxene; review and thermodynamic approach. *American Journal of Science, 293*(2), 111-134. http://www.ajsonline.org/content/293/2/111.short

Nordstrom, D. (1982). Aqueous pyrite oxidation and the consequent formation of secondary minerals. In (Vol. 10, pp. 37-56).

Norini, G., Bustos, E., Arnosio, M., Baez, W., Zuluaga, M. C., and Roverato, M. (2020). Unusual volcanic instability and sector collapse configuration at Chimpa volcano, central Andes. *Journal of Volcanology and Geothermal Research, 393*, 106807. http://www.sciencedirect.com/science/article/pii/S0377027319306377

Nuñez-Hernández, S., Pinti, D. L., López-Hernández, A., Shouakar-Stash, O., Martínez-Cinco, M. A., Abuharara, A., et al. (2020). Phase segregation, boiling, and reinjection at the Los Azufres Geothermal Field, Mexico, monitored by water stable isotopes, chloride, and enthalpy. *Journal of Volcanology and Geothermal Research, 390*, 106751. http://www.sciencedirect.com/science/article/pii/S0377027319300149

Okujeni, A., van der Linden, S., Tits, L., Somers, B., and Hostert, P. (2013). Support vector regression and synthetically mixed training data for quantifying urban land cover. *Remote Sensing of Environment, 137*, 184-197. http://www.sciencedirect.com/science/article/pii/S0034425713002009

Okumura, S., and Sasaki, O. (2014). Permeability reduction of fractured rhyolite in volcanic conduits and its control on eruption cyclicity. *Geology, 42*(10), 843-846. https://doi.org/10.1130/G35855.1

Pal, M. (2005). Random forest classifier for remote sensing classification. *International Journal of Remote Sensing, 26*(1), 217-222. http://dx.doi.org/10.1080/01431160412331269698

1299 Palmer, B. A., and Neall, V. E. (1989). The Murimotu Formation—9500 year old deposits of a debris
1300 avalanche and associated lahars, Mount Ruapehu, North Island, New Zealand. *New Zealand*
1301 *Journal of Geology and Geophysics, 32*(4), 477-486.
1302 https://doi.org/10.1080/00288306.1989.10427555
1303 Pardo, N., Cronin, S., Palmer, A., Procter, J., and Smith, I. (2012). Andesitic Plinian eruptions at Mt.
1304 Ruapehu: quantifying the uppermost limits of eruptive parameters. *Bulletin of Volcanology,*
1305 *74*(5), 1161-1185. http://dx.doi.org/10.1007/s00445-012-0588-y
1306 Pardo, N., Cronin, S. J., Németh, K., Brenna, M., Schipper, C. I., Breard, E., et al. (2014). Perils in
1307 distinguishing phreatic from phreatomagmatic ash; insights into the eruption mechanisms of the
1308 6 August 2012 Mt. Tongariro eruption, New Zealand. *Journal of Volcanology and Geothermal*
1309 *Research, 286*, 397-414. http://www.sciencedirect.com/science/article/pii/S037702731400136X
1310 Piccoli, P. M., and Candela, P. A. (2002). Apatite in Igneous Systems. *Reviews in Mineralogy and*
1311 *Geochemistry, 48*(1), 255-292. https://doi.org/10.2138/rmg.2002.48.6
1312 Piochi, M., Mormone, A., and Balassone, G. (2019). Hydrothermal alteration environments and recent
1313 dynamics of the Ischia volcanic island (southern Italy): Insights from repeated field,
1314 mineralogical and geochemical surveys before and after the 2017 Casamicciola earthquake.
1315 *Journal of Volcanology and Geothermal Research, 376*, 104-124.
1316 http://www.sciencedirect.com/science/article/pii/S0377027318303263
1317 Piochi, M., Mormone, A., Balassone, G., Strauss, H., Troise, C., and De Natale, G. (2015). Native sulfur,
1318 sulfates and sulfides from the active Campi Flegrei volcano (southern Italy): Genetic
1319 environments and degassing dynamics revealed by mineralogy and isotope geochemistry.
1320 *Journal of Volcanology and Geothermal Research, 304*, 180-193.
1321 http://www.sciencedirect.com/science/article/pii/S0377027315002735
1322 Pola, A., Crosta, G. B., Fusi, N., and Castellanza, R. (2014). General characterization of the mechanical
1323 behaviour of different volcanic rocks with respect to alteration. *Engineering Geology, 169*, 1-13.
1324 http://www.sciencedirect.com/science/article/pii/S0013795213003293
1325 Price, R. C., Gamble, J. A., Smith, I. E. M., Maas, R., Waight, T., Stewart, R. B., and Woodhead, J. (2012).
1326 The Anatomy of an Andesite Volcano: a Time–Stratigraphic Study of Andesite Petrogenesis and
1327 Crustal Evolution at Ruapehu Volcano, New Zealand. *Journal of Petrology, 53*(10), 2139-2189.
1328 https://doi.org/10.1093/petrology/egs050
1329 Procter, J. N., Cronin, S. J., Zernack, A. V., Lube, G., Stewart, R. B., Nemeth, K., and Keys, H. (2014). Debris
1330 flow evolution and the activation of an explosive hydrothermal system; Te Maari, Tongariro,
1331 New Zealand. *Journal of Volcanology and Geothermal Research, 286*, 303-316.
1332 http://www.sciencedirect.com/science/article/pii/S0377027314002170
1333 Pu, H.-C., Lin, C.-H., Hsu, Y.-J., Lai, Y.-C., Shih, M.-H., Murase, M., and Chang, L.-C. (2020). Volcano-
1334 hydrothermal inflation revealed through spatial variation in stress field in Tatun Volcano Group,
1335 Northern Taiwan. *Journal of Volcanology and Geothermal Research, 390*, 106712.
1336 http://www.sciencedirect.com/science/article/pii/S0377027319304093
1337 Pullanagari, R. R., Kereszturi, G., and Yule, I. J. (2016). Mapping of macro and micro nutrients of mixed
1338 pastures using airborne AisaFENIX hyperspectral imagery. *ISPRS Journal of Photogrammetry and*
1339 *Remote Sensing, 117*, 1-10.
1340 http://www.sciencedirect.com/science/article/pii/S0924271616000782
1341 Reid, M. E. (2004). Massive collapse of volcano edifices triggered by hydrothermal pressurization.
1342 *Geology, 32*(5), 373-376. http://pubs.er.usgs.gov/publication/70027272
1343 Richter, R., and Schläpfer, D. (2002). Geo-atmospheric processing of airborne imaging spectrometry
1344 data. Part 2: Atmospheric/topographic correction. *International Journal of Remote Sensing,*
1345 *23*(13), 2631-2649. http://dx.doi.org/10.1080/01431160110115834

Roberts, D. A., Gardner, M., Church, R., Ustin, S., Scheer, G., and Green, R. O. (1998). Mapping Chaparral in the Santa Monica Mountains Using Multiple Endmember Spectral Mixture Models. *Remote Sensing of Environment, 65*(3), 267-279. http://www.sciencedirect.com/science/article/pii/S0034425798000376

Rogge, D., Rivard, B., Segl, K., Grant, B., and Feng, J. (2014). Mapping of NiCu–PGE ore hosting ultramafic rocks using airborne and simulated EnMAP hyperspectral imagery, Nunavik, Canada. *Remote Sensing of Environment, 152*(0), 302-317. http://www.sciencedirect.com/science/article/pii/S0034425714002442

Rosas-Carbajal, M., Komorowski, J.-C., Nicollin, F., and Gibert, D. (2016). Volcano electrical tomography unveils edifice collapse hazard linked to hydrothermal system structure and dynamics. *Scientific Reports, 6*(1), 29899. https://doi.org/10.1038/srep29899

Rowan, L. C., and Mars, J. C. (2003). Lithologic mapping in the Mountain Pass, California area using Advanced Spaceborne Thermal Emission and Reflection Radiometer (ASTER) data. *Remote Sensing of Environment, 84*(3), 350-366.

Rowe, G. L., and Brantley, S. L. (1993). Estimation of the dissolution rates of andesitic glass, plagioclase and pyroxene in a flank aquifer of Poás Volcano, Costa Rica. *Chemical Geology, 105*(1), 71-87. http://www.sciencedirect.com/science/article/pii/0009254193901194

Rowlands, D. P., White, R. S., and Haines, A. J. (2005). Seismic tomography of the Tongariro Volcanic Centre, New Zealand. *Geophysical Journal International, 163*(3), 1180-1194. https://doi.org/10.1111/j.1365-246X.2005.02716.x

Rutledge, A. M., Horgan, B. H. N., Havig, J. R., Rampe, E. B., Scudder, N. A., and Hamilton, T. L. (2018). Silica Dissolution and Precipitation in Glaciated Volcanic Environments and Implications for Mars. *Geophysical Research Letters, 45*(15), 7371-7381. https://agupubs.onlinelibrary.wiley.com/doi/abs/10.1029/2018GL078105

Rye, R. O. (2005). A review of the stable-isotope geochemistry of sulfate minerals in selected igneous environments and related hydrothermal systems. *Chemical Geology, 215*(1), 5-36. http://www.sciencedirect.com/science/article/pii/S0009254104003869

Rye, R. O., Bethke, P. M., and Wasserman, M. D. (1992). The stable isotope geochemistry of acid sulfate alteration. *Economic Geology, 87*(2), 225-262. https://doi.org/10.2113/gsecongeo.87.2.225

Schaefer, L. N., Kendrick, J. E., Oommen, T., Lavallée, Y., and Chigna, G. (2015). Geomechanical rock properties of a basaltic volcano. *Frontiers in Earth Science, 3*(29). Original Research. http://journal.frontiersin.org/article/10.3389/feart.2015.00029

Schaefer, L. N., Kennedy, B. M., Villeneuve, M. C., Cook, S. C. W., Jolly, A. D., Keys, H. J. R., and Leonard, G. S. (2018). Stability assessment of the Crater Lake/Te Wai-ā-moe overflow channel at Mt. Ruapehu (New Zealand), and implications for volcanic lake break-out triggers. *Journal of Volcanology and Geothermal Research, 358*, 31-44. http://www.sciencedirect.com/science/article/pii/S0377027318301008

Schläpfer, D., and Richter, R. (2002). Geo-atmospheric processing of airborne imaging spectrometry data. Part 1: Parametric orthorectification. *International Journal of Remote Sensing, 23*(13), 2609-2630. http://dx.doi.org/10.1080/01431160110115825

Schwertmann, U., and Murad, E. (1983). Effect of pH on the Formation of Goethite and Hematite from Ferrihydrite. *Clays and Clay Minerals, 31*(4), 277-284. journal article. https://doi.org/10.1346/CCMN.1983.0310405

Scott, K. M. (1990). Origin of alunite- and jarosite-group minerals in the Mt. Leyshon epithermal gold deposit, Northeast Queensland, Australia. *American Mineralogist, 75*(9-10), 1176-1181.

Sillitoe, R. H., and Hedenquist, J. W. (2003). Linkages between volcanotectonic settings, ore-fluid compositions, and epithermal precious metal deposits. *Special Publication-Society of Economic Geologists, 10*, 315-343.

Simmons, S. F., White, N. C., John, D. A., Hedenquist, J. W., Thompson, J. F. H., Goldfarb, R. J., and Richards, J. P. (2005). Geological Characteristics of Epithermal Precious and Base Metal Deposits. In *One Hundredth Anniversary Volume* (pp. 0): Society of Economic Geologists.

Siratovich, P. A., Heap, M. J., Villeneuve, M. C., Cole, J. W., Kennedy, B. M., Davidson, J., and Reuschlé, T. (2016). Mechanical behaviour of the Rotokawa Andesites (New Zealand): Insight into permeability evolution and stress-induced behaviour in an actively utilised geothermal reservoir. *Geothermics, 64*, 163-179. http://www.sciencedirect.com/science/article/pii/S0375650516300451

Smith, D. J., Naden, J., Jenkin, G. R. T., and Keith, M. (2017). Hydrothermal alteration and fluid pH in alkaline-hosted epithermal systems. *Ore Geology Reviews, 89*, 772-779. http://www.sciencedirect.com/science/article/pii/S0169136817302913

Stern, T. A., Stratford, W. R., and Salmon, M. L. (2006). Subduction evolution and mantle dynamics at a continental margin: Central North Island, New Zealand. *Reviews of Geophysics, 44*(4). https://agupubs.onlinelibrary.wiley.com/doi/abs/10.1029/2005RG000171

Stoffregen, R. E., and Alpers, C. N. (1987). Woodhouseite and svanbergite in hydrothermal ore deposits; products of apatite destruction during advanced argillic alteration. *The Canadian Mineralogist, 25*(2), 201-211.

Streck, M. J., and Dilles, J. H. (1998). Sulfur evolution of oxidized arc magmas as recorded in apatite from a porphyry copper batholith. *Geology, 26*(6), 523-526. https://doi.org/10.1130/0091-7613(1998)026<0523:SEOOAM>2.3.CO;2

Swayze, G. A., Clark, R. N., Goetz, A. F. H., Livo, K. E., Breit, G. N., Kruse, F. A., et al. (2014). Mapping Advanced Argillic Alteration at Cuprite, Nevada, Using Imaging Spectroscopy. *Economic Geology, 109*(5), 1179-1221. http://economicgeology.org/content/109/5/1179.abstract

Ta, K., Peng, X., Chen, S., Xu, H., Li, J., Du, M., et al. (2017). Hydrothermal nontronite formation associated with microbes from low-temperature diffuse hydrothermal vents at the South Mid-Atlantic Ridge. *Journal of Geophysical Research: Biogeosciences, 122*(9), 2375-2392.

Tan, W., Liu, P., He, H., Wang, C. Y., and Liang, X. (2016). Mineralogy and Origin of Exsolution in Ti-rich Magnetite from Different Magmatic Fe-ti Oxide-bearing Intrusions. *The Canadian Mineralogist, 54*(3), 539-553. https://doi.org/10.3749/canmin.1400069

Tost, M., Cronin, S. J., Procter, J. N., Smith, I. E. M., Neall, V. E., and Price, R. C. (2015). Impacts of catastrophic volcanic collapse on the erosion and morphology of a distal fluvial landscape: Hautapu River, Mount Ruapehu, New Zealand. *Geological Society of America Bulletin, 127*(1-2), 266-280. http://gsabulletin.gsapubs.org/content/127/1-2/266.abstract

Townsend, D. B., Leonard, G. S., Conway, C. E., Eaves, S. R., Wilson, C. J. N., and compilers. (2017). Geology of the Tongariro National Park area [scale 1:60 000 map]. In *GNS Science geological map; 4* (pp. 1 sheet + 109 p.,). Lower Hutt, New Zealand: GNS Science.

van der Meer, F. (2004). Analysis of spectral absorption features in hyperspectral imagery. *International Journal of Applied Earth Observation and Geoinformation, 5*(1), 55-68. http://www.sciencedirect.com/science/article/pii/S0303243403000382

van der Meer, F., Kopačková, V., Koucká, L., van der Werff, H. M. A., van Ruitenbeek, F. J. A., and Bakker, W. H. (2018). Wavelength feature mapping as a proxy to mineral chemistry for investigating geologic systems: An example from the Rodalquilar epithermal system. *International Journal of Applied Earth Observation and Geoinformation, 64*, 237-248. http://www.sciencedirect.com/science/article/pii/S0303243417301976

van Hinsberg, V., Berlo, K., van Bergen, M., and Williams-Jones, A. (2010). Extreme alteration by hyperacidic brines at Kawah Ijen volcano, East Java, Indonesia: I. Textural and mineralogical imprint. *Journal of Volcanology and Geothermal Research, 198*(1), 253-263. http://www.sciencedirect.com/science/article/pii/S037702731000288X

Vasconcelos, P. M., and Conroy, M. (2003). Geochronology of weathering and landscape evolution, Dugald River valley, NW Queensland, Australia. *Geochimica et Cosmochimica Acta, 67*(16), 2913-2930. http://www.sciencedirect.com/science/article/pii/S0016703702013728

Wallace, L. M., Beavan, J., McCaffrey, R., and Darby, D. (2004). Subduction zone coupling and tectonic block rotations in the North Island, New Zealand. *Journal of Geophysical Research: Solid Earth, 109*(B12). https://agupubs.onlinelibrary.wiley.com/doi/abs/10.1029/2004JB003241

Watters, R. J., Delahaut, W. D., Haneberg, W. C., and Anderson, S. A. (1995). Effect of argillic alteration on rock mass stability. In *Clay and Shale Slope Instability* (Vol. 10, pp. 0): Geological Society of America.

Westoby, M. J., Brasington, J., Glasser, N. F., Hambrey, M. J., and Reynolds, J. M. (2012). 'Structure-from-Motion' photogrammetry: A low-cost, effective tool for geoscience applications. *Geomorphology, 179*, 300-314. http://www.sciencedirect.com/science/article/pii/S0169555X12004217

Wright, R., Flynn, L. P., and Harris, A. J. L. (2001). Evolution of lava flow-fields at Mount Etna, 27-28 October 1999, observed by Landsat 7 ETM+. *Bulletin of Volcanology, 63*(1), 1-7. http://www.scopus.com/inward/record.url?eid=2-s2.0-0034925245&partnerID=40&md5=a47b808c2afe4cd05f7e7792e9a9d6af

Wyering, L. D., Villeneuve, M. C., Wallis, I. C., Siratovich, P. A., Kennedy, B. M., Gravley, D. M., and Cant, J. L. (2014). Mechanical and physical properties of hydrothermally altered rocks, Taupo Volcanic Zone, New Zealand. *Journal of Volcanology and Geothermal Research, 288*, 76-93. http://www.sciencedirect.com/science/article/pii/S0377027314003060

Zabcic, N., Rivard, B., Ong, C., and Mueller, A. (2014). Using airborne hyperspectral data to characterize the surface pH and mineralogy of pyrite mine tailings. *International Journal of Applied Earth Observation and Geoinformation, 32*(0), 152-162. http://www.sciencedirect.com/science/article/pii/S0303243414000920

Zimbelman, D. R., Rye, R. O., and Breit, G. N. (2005). Origin of secondary sulfate minerals on active andesitic stratovolcanoes. *Chemical Geology, 215*(1), 37-60. http://www.sciencedirect.com/science/article/pii/S0009254104003870

Zolotov, M. Y., and Shock, E. L. (2005). Formation of jarosite-bearing deposits through aqueous oxidation of pyrite at Meridiani Planum, Mars. *Geophysical Research Letters, 32*(21). https://agupubs.onlinelibrary.wiley.com/doi/abs/10.1029/2005GL024253